J. Fluid Mech. (2007), *vol.* 573, *pp.* 265–295. © 2007 Cambridge University Press
doi:10.1017/S0022112006003806 Printed in the United Kingdom

Proper orthogonal decomposition and low-dimensional modelling of thermally driven two-dimensional flow in a horizontal rotating cylinder

NADEEM HASAN[1] AND SANJEEV SANGHI[2]

[1]Department of Mechanical Engineering, Aligarh Muslim University, Aligarh, India

[2]Department of Applied Mechanics, Indian Institute of Technology Delhi, New Delhi, India

(Received 9 May 2005 and in revised form 17 August 2006)

A proper orthogonal decomposition (POD) analysis and low-dimensional modelling of thermally driven two-dimensional flow of air in a horizontal rotating cylinder, subject to the Boussinesq approximation, is considered. The problem is unsteady due to the harmonic nature of the gravitational buoyancy force with respect to the rotating observer and is characterized by four dimensionless numbers: gravitational Rayleigh number (Ra_g), the rotational Rayleigh number (Ra_Ω), the Taylor number (Ta) and Prandtl number (Pr). The data for the POD analysis are obtained by numerical integration of the governing equations of mass, momentum and energy. The POD is applied to the computational data for Ra_Ω varying in the range 10^2–10^6 while Ra_g and Pr are fixed at 10^5 and 0.71 respectively. The ratio of Ta to Ra_Ω is fixed at 100 so that the results apply to physically realistic situations. A new criterion, in the form of appropriately defined error norms, for assessing the truncation error of the POD expansion is proposed. It is shown that these error norms reflect the accuracy of the POD-based reconstructions of a given data ensemble better than the widely employed average energy criterion. The translational symmetry in both space and time of the pair of modes having degenerate (equal) eigenvalues confirms the presence of travelling waves in the flow for several different Ra_Ω values. The shifts in space and time of the structure of the degenerate modes are utilized to estimate the wave speeds in a given direction. The governing equations for the fluctuations are derived and low-dimensional models are constructed by employing a Galerkin procedure. For each of the five values of Ra_Ω, the low-dimensional models yield accurate qualitative as well as quantitative behaviour of the system. Sufficient modes are included in the low-dimensional models so that the modelling of the unresolved scales of motion is not needed to stabilize their solution. Not more than 20 modes are required in the low-dimensional models to accurately model the system dynamics. The ability of low-dimensional models to accurately predict the system behaviour for a set of parameters different from those from which they were constructed is also examined.

1. Introduction

The proper orthogonal (POD) or Karhunen–Loève (K–L) decomposition is an established technique for extracting the most 'energetic' or dominant spatial structures in the average sense from an ensemble of functions representing an infinite-dimensional process. Once the spatial structure of the ensemble is captured

in the spatial basis functions or modes, the members of the ensemble can be represented as linear superpositions of these modes. The advantage of using the proper orthogonal or K-L basis is that finite truncations of the modal expansion of the ensemble members yield the smallest error in the mean-square sense compared to the other possible orthogonal bases having the same dimension. In the context of fluid mechanics, this means that the structure of a complex spatio-temporal field like the velocity field could be captured in an average sense by a relatively small number of POD modes. If the partial differential equations, like the Navier–Stokes equations, governing the fluid flow are projected onto these spatial POD modes, a system of ordinary differential equations for the temporal coefficients is obtained. Hence, the time evolution of the system could be studied in a state space involving few degrees of freedom, making it easier to investigate the underlying physics.

1.1. *Related literature*

The earliest attempts to apply the above ideas in studying fluid motions were in the context of identifying and studying the role and dynamics of large-scale average spatial structures of the fluctuating velocity field of a turbulent flow. The POD provides an objective way of identifying such structures. The extraction of dominant spatial structures using POD in classical turbulent shear flows has been discussed in the works of Bakewell & Lumley (1967), Herzog (1986), Glauser & George (1987) and Kirby, Boris & Sirovich (1990). Low-dimensional models based on POD have been developed by Aubry *et al.* (1988), Sanghi & Aubry (1993), Moin & Moser (1989) and Sirovich & Park (1990).

Most of the studies involving POD and low-dimensional modelling have been performed on turbulent flows. There have been very few involving the application of POD to unsteady laminar flows where the unsteadiness is either due to inherent instabilities or due to some unsteady forcing. More recently, however, applications of POD to problems like driven cavity flows and flow past bluff bodies have appeared in literature; see for Cazemier, Verstappen & Veldman (1998), Ma & Karniadakis (2002) and Galleti *et al.* (2004).

There are few studies involving the application of POD and POD–Galerkin modelling of flows with heat transfer. Turbulent Rayleigh–Bénard convection problems were considered by Sirovich & Park (1990) and Sirovich & Deane (1991). Deane & Sirovich (1991) investigated the change in the structure of the flow field with increase in Ra for chaotic Rayleigh–Bènard convection. Sahan, Liakopoulos & Gunes (1997) identified the organized spatio-temporal structures in transitional flow with heat transfer in a periodically grooved channel. In that study, the buoyancy effects were neglected and the eigenfunctions for velocity and thermal fields were calculated separately. Low-dimensional models based on four modes yielded accurate results. Podvin & Le Quéré (2001) investigated the two-dimensional buoyancy-driven flow of air in a differentially heated tall cavity. They employed a coupled type of decomposition, where composite vector eigenfunctions having components representing the velocity and thermal fields were obtained. For a slightly supercritical Rayleigh number they have shown that a two-mode model captures the dynamics reasonably accurately. At some distance from the critical point the flow becomes chaotic and a ten-dimensional model successfully captures the dynamics. Thus, POD analysis and the associated low-dimensional modelling is an effective reduction tool not only for turbulent flows but also for transitional laminar flows.

The next subsection briefly introduces the problem previously investigated by the present authors that is the subject of the POD analysis and low-dimensional modelling in the present work.

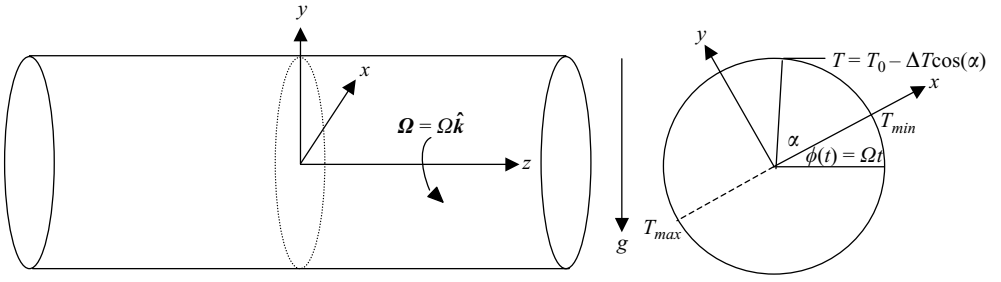

FIGURE 1. Geometry of the problem.

1.2. *Thermally driven flow in a steadily rotating horizontal cylinder*

This work applies POD and POD–Galerkin models to study the problem of two-dimensional thermally driven flow in a horizontal steadily rotating cylinder. The problem has applications in thermal energy storage systems undergoing rotation and in the design of cooling systems for rotating machinery. The problem has been investigated numerically by Hasan & Sanghi (2004, hereafter referred to as HS). A Cartesian frame of reference attached to the rotating cylinder was employed in the study. To an observer attached to the cylinder, the gravity vector rotates, resulting in a time-periodic gravitational buoyancy force driving the flow. Thus, the problem involves unsteady forcing and is therefore inherently unsteady in nature. It is assumed that the cylinder has been rotating steadily for a sufficient length of time that the fluid is in a state of solid-body rotation under isothermal conditions. A temperature perturbation in the form of a periodic cosine function of the angular location of a spatial point is imposed on the wall of the cylinder, as shown in figure 1. The fluid motion relative to the rotating cylinder is induced by the combined action of gravitational buoyancy (GB) and centrifugal or rotational buoyancy (RB). The dimensionless governing equations of mass, momentum and energy subject to the Boussinesq approximation in a Cartesian frame rotating with the cylinder are

mass

$$\nabla \cdot \boldsymbol{V} = 0, \tag{1}$$

momentum

$$\frac{\mathrm{D}\boldsymbol{V}}{\mathrm{D}\tau} = -\nabla p_m - Ra_g Pr\,\theta\,\hat{\boldsymbol{n}}_g - Ra_\Omega Pr\,\theta \boldsymbol{r} - 2Ta^{1/2}Pr(\hat{\boldsymbol{k}} \times \boldsymbol{V}) + Pr\nabla^2 \boldsymbol{V}, \tag{2}$$

energy equation

$$\frac{\mathrm{D}\theta}{\mathrm{D}\tau} = \nabla^2 \theta. \tag{3}$$

The vector $\hat{\boldsymbol{n}}_g$ in (2) is the unit vector indicating the instantaneous direction of the rotating gravity vector and is defined as

$$\hat{\boldsymbol{n}}_g = -\hat{\boldsymbol{i}} \sin\left(Ta^{1/2}Pr\,\tau\right) - \hat{\boldsymbol{j}} \cos\left(Ta^{1/2}Pr\,\tau\right).$$

The length, time and velocity scales employed to transform the equations to their dimensionless forms are R, R^2/κ and κ/R respectively, where the cylinder radius is R and the thermal diffusivity of the fluid κ. The term p_m in (2) is the dimensionless change in pressure with respect to the pressure in the solid-body rotation state under isothermal conditions. This is the rotational analogue of piezometric pressure. The temperature in the governing equations appears in the form of a dimensionless change

with respect to the isothermal conditions that prevail prior to the application of the temperature perturbation at the wall. The formal definitions of p_m and θ are

$$p_m = \frac{(P - P_0)R^2}{\rho_0 \kappa^2}, \qquad \theta = \frac{(T - T_0)}{\Delta T}. \tag{4}$$

In the solid–body rotation state, the fluid is taken to be at a uniform temperature T_0 and density ρ_0. The amplitude of the periodic temperature perturbation is represented as ΔT. The dimensional pressure P_0 in a state of rest with respect to the rotating frame under isothermal conditions is given by the momentum equation as

$$\nabla P_0 = \rho_0(\boldsymbol{g} - \boldsymbol{\Omega} \times \boldsymbol{\Omega} \times \boldsymbol{r}), \tag{5}$$

where $\boldsymbol{\Omega}$ is the steady rotation rate of the frame attached to the rotating cylinder. Equations (1)–(3) together with the no-slip boundary conditions for the velocity and the specified temperature perturbation (figure 1), govern the motion of the fluid relative to the rotating frame. From (2) it is readily seen that the relative motion can be induced by buoyancy forces associated with the gravity and the centrifugal accelerations.

Some remarks on the two-dimensional flow assumption are worth making. In a steadily rotating cylinder under isothermal conditions, the state of solid-body rotation would exist. If the cylinder is assumed to be sufficiently long, then excluding the end effects, the imposed temperature perturbation (figure 1) generates the buoyancy forces (gravitational and rotational) whose variation along the cylinder axis (z-direction, figure 1) may be neglected. Thus these buoyancy forces induce a fluid motion, relative to the solid-body rotation, that can be approximated as two-dimensional in character provided the end effects are neglected. As the rotation axis is perpendicular to the gravity vector, the buoyancy forces are confined to the cross-sectional planes, thereby inducing an approximately two-dimensional fluid motion confined to the cross-sectional planes in the central portion of the cylinder. For such an induced velocity field, the Coriolis force, as seen from (2), lies completely in the (x-y)-plane and does not induce any motion in the z-direction. Hamady *et al.* (1994), working with a rotating square-cross-section cylinder having a length 10 times the edge of the cross-section, found excellent agreement between experimental and numerical results on the basis of two-dimensional numerical computations.

An interesting observation can be made regarding the role of the Coriolis force for the problem under consideration. It can be readily verified from (2) that the Coriolis force is irrotational in character. This is primarily due to the two-dimensional approximation of the flow field and the Boussinesq approximation that constrains the velocity field to be divergence free. The irrotational character implies that the Coriolis force combines with the pressure field to generate an effective pressure field that, for the present problem, evolves as a function of the velocity and the thermal fields. Thus the Coriolis force only affects the pressure field and does not play any role in the evolution of the velocity and the thermal fields.

The dimensionless system (1)–(3) has four dimensionless parameters, namely (i) gravitational Rayleigh number (Ra_g), (ii) Rotational Rayleigh number (Ra_Ω), (iii) Taylor number (Ta) and (iv) Prandtl number (Pr). These are defined as

$$Ra_g = \frac{g\beta\Delta T R^3}{\nu\kappa}, \quad Ra_\Omega = \frac{\Omega^2\beta\Delta T R^4}{\nu\kappa}, \quad Ta = \frac{\Omega^2 R^4}{\nu^2}, \quad Pr = \frac{\nu}{\kappa}, \tag{6}$$

where β and ν are the coefficient of volume expansion and the kinematic viscosity of the fluid respectively, while g and Ω are the acceleration due to gravity and the steady rotation rate of the cylinder.

It was shown by Ker & Lin (1996) that, in order to obtain physically realizable solutions, it is important to recognize that the ratio Ta/Ra_Ω from (6) is equal to $1/(\beta\,\Delta T\,Pr)$. Therefore, while the parameters Ra_g and Ra_Ω can be varied independently, the values of Ta must be chosen so that the ratio is maintained within practical limits. The numerical investigation by HS was carried out at a fixed $Ra_g = 10^5$ and $Pr = 0.71$, while Ra_Ω was varied from 10^2 to 10^6. The ratio of Ta and Ra_Ω was fixed at 100. As an aid to understanding the results obtained from the POD analysis and low-dimensional models in the present study, the main computational findings of the numerical investigation performed earlier by the authors are presented in the next section.

1.3. *Summary of the computational findings*

The computational study of HS correlated the spatio-temporal dynamics and the heat transfer characteristics to the changes in Ra_Ω and Ta over a wide range at a fixed $Ra_g = 10^5$ and $Pr = 0.71$. The computational study revealed that for $Ra_\Omega < 10^5$ the spatial structure of the flow is quite sensitive to the changing orientation of the gravity vector in the rotating frame. The flow exhibits a periodic behaviour with frequency locked onto the rotation frequency of the gravity vector with temporal variations in the flow caused by harmonic forcing of the gravitational buoyancy force. For $Ra_\Omega > 10^5$, the large-scale spatial structure of the flow is quite insensitive to the harmonic time-varying gravitational buoyancy force. Examination of the temporal structure via fast Fourier transformation (FFT) revealed bifurcations from periodic to quasi-periodic states for $Ra_\Omega \in [10^6, 10^7]$. It was shown that the mean heat transfer characteristic is highly non-monotonic, indicating the aiding and mitigating effects of rotation on convection in different ranges of Ra_Ω. At low rotation rates ($Ra_\Omega \sim 10^3$), the flow is governed essentially by the gravitational buoyancy force with large amplitudes of fluctuation, while the centrifugal effects were found to be negligible. As Ra_Ω is increased, the role of gravity progressively diminishes and the fluctuation levels become extremely small to render the flow almost as steady as Ra_Ω approaches a value of 10^5. The flow for $Ra_\Omega \in [5 \times 10^5, 10^7]$ is driven essentially by the centrifugal or rotational buoyancy forces. In this range, the large-scale flow structure consists of a two-cell convection with the interface of the cells aligned along the horizontal diameter, and an increase in Ra_Ω brings about an increase in convection. The two cells become increasingly distorted and multiple rolls appear, as an outcome of bifurcations to quasi-periodic states, as Ra_Ω approaches 10^7. In the range given by $2 \times 10^3 \leqslant Ra_\Omega \leqslant 5 \times 10^5$, the flow is controlled by both the body forces. Under the competing influence of the two buoyancy forces, it is shown that the convection is in general suppressed, with very low flow velocities and associated heat transfer.

To summarize, the flow problem chosen exhibits a rich and diverse flow behaviour owing to the presence of: (*a*) multiple driving forces and (*b*) an unsteady driving force. Further, in the gravity-dominated flow regime, the amplitude as well as frequency of the unsteady buoyancy force combine to generate interesting flow dynamics.

The current study is motivated by the fact that, for a complex unsteady flow such as the one under consideration, the POD analysis can provide useful information regarding the flow physics by representing the flow in terms of few modes. Furthermore, it is of interest to examine the feasibility of constructing low-dimensional models and to assess the performance of such models, particularly for flows driven

by unsteady forces. The procedure for carrying out the decomposition and the results of the decomposition are presented in the next section.

2. POD analysis

2.1. *Numerical simulations*

The data for carrying out the POD analysis and the construction of low-dimensional models are taken from the numerical study of HS. The scheme has been described in detail in HS and in Hasan, Anwer & Sanghi (2005).

The numerical integration of (1)–(3) was performed through a semi-explicit pressure correction scheme as described by Hirsch (1990). The discretization is of finite-difference type on a Cartesian colocated grid. The scheme is first-order accurate in time. A second-order central differencing is employed for the convective terms near boundary points while a hybrid third-order upwinding or fourth-order central differencing depending on the local cell Péclet number is utilized in the interior. The diffusion terms are discretized by employing a fourth-order symmetric five-point stencil in the interior and a second-order symmetric three-point stencil near the boundary. The pressure gradient terms in the momentum equations are discretized using a two-point central differencing stencil.

The boundary of the flow domain under consideration is a solid impervious boundary. Thus no-slip conditions for velocity are specified at the wall of the cylinder. The temperature is specified in the form of a periodic distribution:

$$\theta = -cos(\alpha).$$

The pressure at the wall is obtained by applying the normal momentum equation.

2.2. *Proper orthogonal decomposition: theory*

Let $\boldsymbol{U}^m = \boldsymbol{U}(\boldsymbol{x}, \tau_m)$, $m = 1, \ldots, M$ be M realizations or snapshots of the fluctuating flow field obtained through experimentation or numerical simulations. In the present case, the snapshot $\boldsymbol{U}^m \equiv (U_1, U_2, U_3)^m$ comprises both the fluctuating velocity components ($U_1 = u'$, $U_2 = v'$) and the fluctuating temperature field ($U_3 = \theta'$) assigned at each point. The K-L basis functions $\boldsymbol{\phi}$ are taken to be vector functions with three components at each point (ϕ_1, ϕ_2, ϕ_3) associated with the two velocity components and the thermal field. The vector space in which the decomposition is sought has an inner product defined as

$$(\boldsymbol{f}, \boldsymbol{g}) = \int_D (f_1 g_1 + f_2 g_2 + \gamma f_3 g_3)\, \mathrm{d}A.$$

As pointed out by Lumley & Poje (1997), the introduction of a scaling factor γ is necessary to balance the velocity and temperature fluctuation energies so that the K-L basis captures the structure of the most energetic fluctuations of both the temperature and the velocity fields in a composite manner. They have shown that the proper value of γ that maximizes the average of the square of the projection of the data onto the basis function $\boldsymbol{\phi}$ is

$$\gamma = \frac{\displaystyle\int_\Omega \langle (u'u' + v'v') \rangle \, \mathrm{d}A}{\displaystyle\int_\Omega \langle \theta'\theta' \rangle \, \mathrm{d}A}, \tag{7}$$

The K-L basis function $\boldsymbol{\phi}$ is governed by the integral eigenvalue problem

$$\int_\Omega R_{ij}(x, x')\, \phi_j(x')\, \mathrm{d}A = \lambda \phi_i(x), \quad (i, j) \in \{1, 3\}, \tag{8}$$

Mode number	Value	Snapshots = 16	32	64	128
1	$\lambda^{(1)} \times 10^{-4}$	1.453	1.453	1.453	1.453
2	$\lambda^{(2)} \times 10^{-3}$	4.726	4.724	4.724	4.724
3	$\lambda^{(3)} \times 10^{-3}$	2.119	2.118	2.118	2.118
4	$\lambda^{(4)} \times 10^{-2}$	7.671	7.664	7.664	7.664
5	$\lambda^{(5)} \times 10^{-2}$	2.462	2.456	2.456	2.456
6	$\lambda^{(6)} \times 10^{-2}$	2.199	2.151	2.151	2.151
7	$\lambda^{(7)} \times 10^{-1}$	8.446	8.444	8.444	8.444
8	$\lambda^{(8)} \times 10^{-1}$	6.616	6.288	6.286	6.286
9	$\lambda^{(9)} \times 10^{-1}$	4.663	4.074	4.073	4.073
10	$\lambda^{(10)} \times 10^{-1}$	2.810	2.353	2.353	2.352

TABLE 1. Convergence of the first ten eigenvalues with increasing number of snapshots at $Ra_\Omega = 10^2$.

where

$$R_{ij}(x, x') = \langle U_i(x, \tau) U_j(x', \tau) \rangle.$$

The eigenvalue problem in (8) yields a countably infinite orthogonal set of eigenfunctions $\{\boldsymbol{\phi}\}_1^\infty$ and non-negative eigenvalues $\{\lambda\}_1^\infty$ (Holmes, Lumley & Berkooz 1996). The K-L basis is utilized for carrying out the decomposition of the flow field as

$$\boldsymbol{U}(\boldsymbol{x}, \tau) = \sum_1^\infty a^{(p)}(\tau) \boldsymbol{\phi}^{(p)}(\boldsymbol{x}). \tag{9}$$

Once the eigenfunctions are known and normalized such that $(\boldsymbol{\phi}^{(p)}, \boldsymbol{\phi}^{(p)}) = 1.0$, the temporal coefficients in (9) can be readily obtained as

$$a^{(p)}(\tau) = \left(\boldsymbol{U}, \boldsymbol{\phi}^{(p)}\right). \tag{10}$$

The total energy captured by the expansion in the average sense is

$$E = \langle (\boldsymbol{U}, \boldsymbol{U}) \rangle = \sum_p \sum_r \left\langle a^{(p)} a^{(r)} \right\rangle \left(\boldsymbol{\phi}^{(p)}, \boldsymbol{\phi}^{(r)}\right) = \sum \lambda^{(p)}. \tag{11}$$

If the eigenvalues $\{\lambda\}_1^\infty$ are ordered such that $\lambda^{(1)} > \lambda^{(2)} > \lambda^{(3)} \ldots$, the sequence on the right of (9) converges more rapidly than with any other basis. The most commonly employed criteria for truncating the infinite sequence in (9) is the retention of the number of modes which capture more than 90 % of the average energy in the ensemble $\boldsymbol{U}^i$ with the condition that none of the neglected modes has more than 1 % of the energy of the most energetic mode (Deane & Sirovich 1991).

In this work, the eigenfunctions $\boldsymbol{\phi}$ have been determined using the method of snapshots proposed by Sirovich (1987).

2.3. *POD results*

From this point onwards, unless stated otherwise, it is understood that 'snapshot' refers to the instantaneous spatial distribution of the fluctuating flow field. For each of the cases, the number of snapshots adequate for the decomposition is determined by carrying out a snapshot independence study. A typical outcome is shown in table 1 for the case of $Ra_\Omega = 10^2$. It can be observed that the leading ten eigenvalues do not change significantly for 32 snapshots or more. A similar study is carried out for other cases of Ra_Ω. For the periodic flows found to occur for $Ra_\Omega = 10^2 - 10^5$, 32

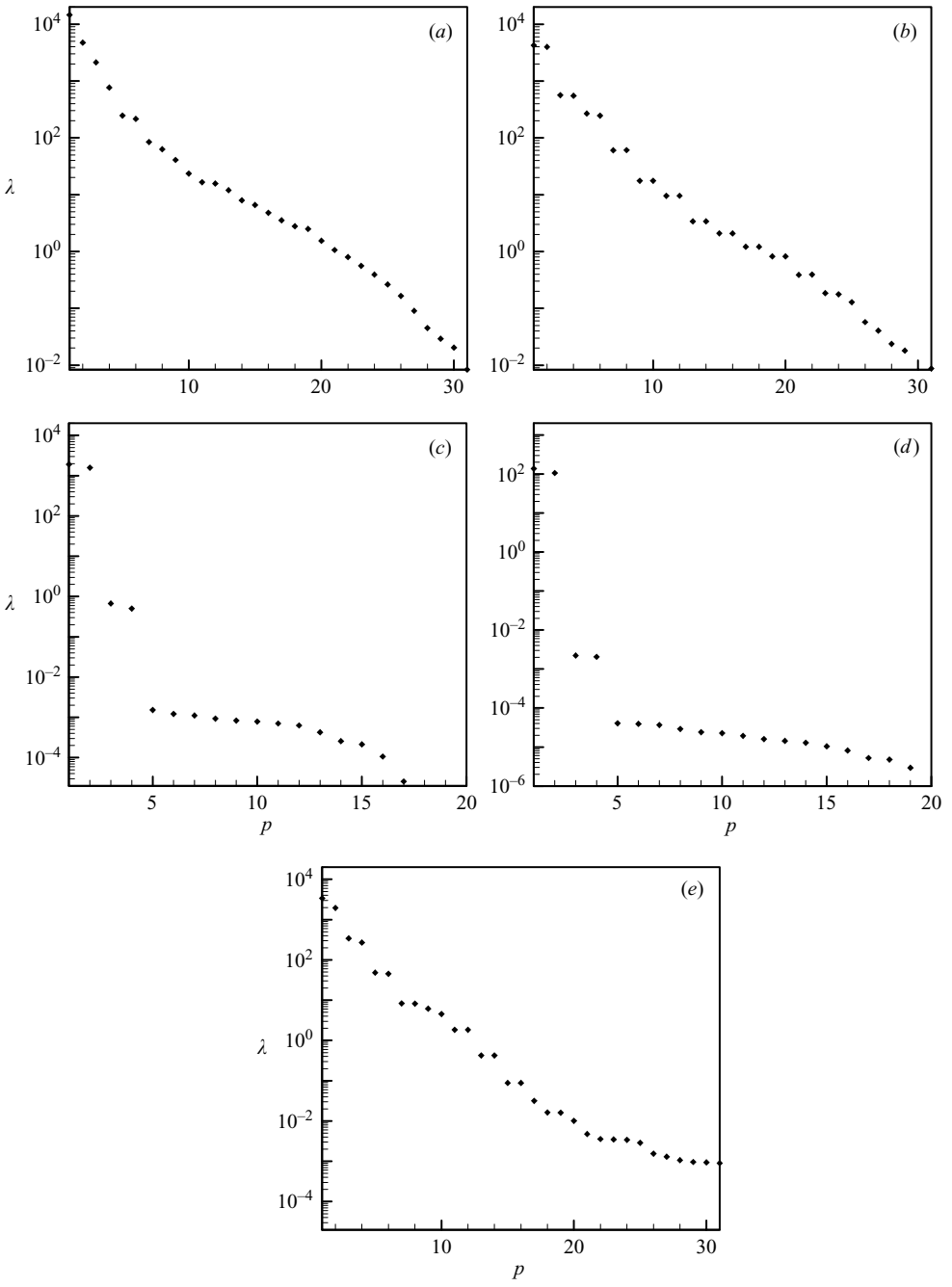

FIGURE 2. Eigenvalue spectra at (*a*) $Ra_\Omega = 10^2$, (*b*) $Ra_\Omega = 10^3$, (*c*) $Ra_\Omega = 10^4$, (*d*) $Ra_\Omega = 10^5$ and (*e*) $Ra_\Omega = 10^6$.

snapshots have been taken for the determination of the modes or eigenfunctions. For the quasi-periodic case of $Ra_\Omega = 10^6$, a set of 400 snapshots has been employed.

Figures 2(*a*)–2(*e*) show the eigenvalue spectra for different value of Ra_Ω. The fast convergence of POD modes is readily shown by the fact that a small number of

modes is needed to capture almost 99 % of the energy of the snapshots in the average sense. The fraction of energy captured by first N modes is

$$E_N/E = \sum_{1}^{N} \lambda^{(p)} \Big/ \sum_{1}^{M} \lambda^{(p)}.$$

At $Ra_\Omega = 10^2$, seven modes capture more than 99 % of the total energy; for $Ra_\Omega = 10^3$, eight modes are needed. For $Ra_\Omega = 10^4$ and $Ra_\Omega = 10^5$ only two modes are sufficient, since as discussed earlier the flow is almost steady for these two cases. For $Ra_\Omega = 10^6$, only six modes are needed.

Note that the eigenspectra for $Ra_\Omega = 10^4$ and $Ra_\Omega = 10^5$ (figure 2(*c*) and figure 2(*d*)) exhibit two dominant modes whose energy content is much higher than the remaining modes. This reflects the fact that the structure of the unsteady flow is relatively simple and is the outcome of the dynamic evolution and interaction of only a few scales of motion.

The cut-off criterion based on average energy does not directly reflect the accuracy with which the corresponding number of modes can be used to reconstruct the original data ensemble or snapshots. This is even more significant for flows involving combined decompositions of fields fundamentally different in character such as the velocity and the thermal fields in the present study. The POD reconstructions of the velocity and thermal fields may converge at different rates and a single lumped criterion based on average energy may not be able to reflect this. In this work we propose a different approach for specifying the cut-off limits for the truncation of the expansion in (9). Let $\boldsymbol{V}^N$ be the fluctuating flow field reconstructed by retaining the first N modes of the expansion in (9). The temporal coefficients required for the evaluation of the expansion are obtained using equation (10). The error norms, E_j^N, $j = 1$, 2 or 3, representing the accuracy of the spatial structure of a given snapshot $\boldsymbol{U}$ obtained via reconstruction using the leading 'N' POD modes, are defined as

$$E_j^N = \left(\int_\Omega \left(U_j - V_j^N \right)^2 \mathrm{d}A \Big/ \int_\Omega U_j^2 \, \mathrm{d}A \right)^{1/2}, \quad j = 1, \text{ 2 or 3.} \tag{12}$$

This is a quantitative measure that reflects directly the accuracy of the reconstruction. These error norms are evaluated for the entire data ensemble comprising M snapshots for a fixed number of POD modes. The maximum values of these error norms ($E_{1\max}^N$, $E_{2\max}^N$, $E_{3\max}^N$) over the entire data ensemble for a given number of modes are taken as a quantitative measure of accuracy with which the data ensemble can be represented with a given number of modes. By specifying limits on these error norms, the number of modes that will provide a reconstruction within a specified level of accuracy over the entire time interval of the data ensemble can be determined. Such a procedure has not been utilized in earlier works involving non-turbulent flows and its significance is shown in this work.

Table 2 shows the number of POD modes or dimensions needed for accurate representation of the data for different cases of Ra_Ω. As expected the error decreases quite rapidly with increase in the number of modes. An interesting comparison between the maximum values of the three error norms, the fraction of average energy captured by a given number of POD modes (N), is also presented in table 2. For $Ra_\Omega = 10^2$, five modes capture 97.798 % of the total energy while the error norms indicate that reconstructions of the fluctuating flow field using five modes yields significant maximum r.m.s. deviations of 36.49 %, 29.80 % and 23.98 % in the velocity components and the temperature field respectively. This shows that the

Ra_Ω	N	E^N_{1max}	E^N_{2max}	E^N_{3max}	$\sum_1^N \lambda^{(p)}/\Sigma\lambda$
	1	1.28799	1.28153	1.05764	0.63481
	5	0.36491	0.29804	0.23976	0.97798
10^2	10	0.11922	0.13242	0.12177	0.99663
	15	0.05463	0.04679	0.06110	0.99919
	20	0.02302	0.02225	0.03037	0.99985
	1	1.03513	1.02374	1.00630	0.42257
	5	0.72120	0.41420	0.25363	0.95644
10^3	10	0.16260	0.08538	0.06714	0.99646
	15	0.05231	0.03749	0.03687	0.99925
	20	0.02511	0.01600	0.01449	0.99986
	1	0.99894	1.02038	1.00424	0.54778
	2	0.01832	0.02856	0.02924	0.99967
10^4	3	0.01163	0.01172	0.02211	0.99986
	4	0.00065	0.00088	0.00094	1.00000
	1	1.00238	1.00410	0.99986	0.56526
	2	0.00411	0.00479	0.00515	0.99998
10^5	3	0.00338	0.00287	0.00501	0.99999
	4	0.00006	0.00006	0.00005	1.00000
	1	1.00902	1.00063	1.00303	0.55686
10^6	5	0.17141	0.17715	0.21381	0.98728
	10	0.02596	0.03273	0.04427	0.99920

TABLE 2. Convergence characteristics of the POD expansion and the variation in the error norms with increase in the number of modes for different Ra_Ω.

energy criterion can be misleading as far as accuracy of the reconstruction of the data ensemble is concerned. A similar observation can be made for all the other cases. The maximum r.m.s. deviations are brought close to 5 % or less by the number of modes that capture greater than 99.9 % of the average energy. Thus, to achieve an accurate reconstruction of the flow under consideration a 99.9 % energy criterion appears suitable. However, while the energy criterion may vary from problem to problem and is hard to predict *a priori*, the criterion based on error norms allows one to achieve any desired level of accuracy in POD reconstructions. The fact that the velocity and thermal fields converge at different rates is also illustrated clearly in table 2. Consider the reconstruction of the flow field at $Ra_\Omega = 10^3$ using 10 modes. The values of the error norms are 16.26 %, 8.54 % and 6.7 %. From the energy criterion, 10 modes capture 99.6 % of the energy with only 0.22 % of the energy in the neglected 11th mode. The energy criterion, therefore, gives a false sense of accuracy. Further, a single lumped criterion is not sensitive to the difference in the convergence rates of the velocity and the thermal fields.

From a qualitative viewpoint, it can be shown that the spatial structure of the instantaneous flow field as obtained by direct numerical simulations (DNS) can be captured using only few modes. Figure 3 shows the flow-field reconstruction for the case of $Ra_\Omega = 10^2$. From a qualitative viewpoint, 10 modes appear to capture the instantaneous flow structure very well. For the case of $Ra_\Omega = 10^4$, only two modes capture the structure of the instantaneous flow field quite accurately (figure 4). It is evident from these figures that the large-scale structure of the unsteady flow field is captured quite well by a small number of modes. At $Ra_\Omega = 10^6$, the flow is quasi-periodic and

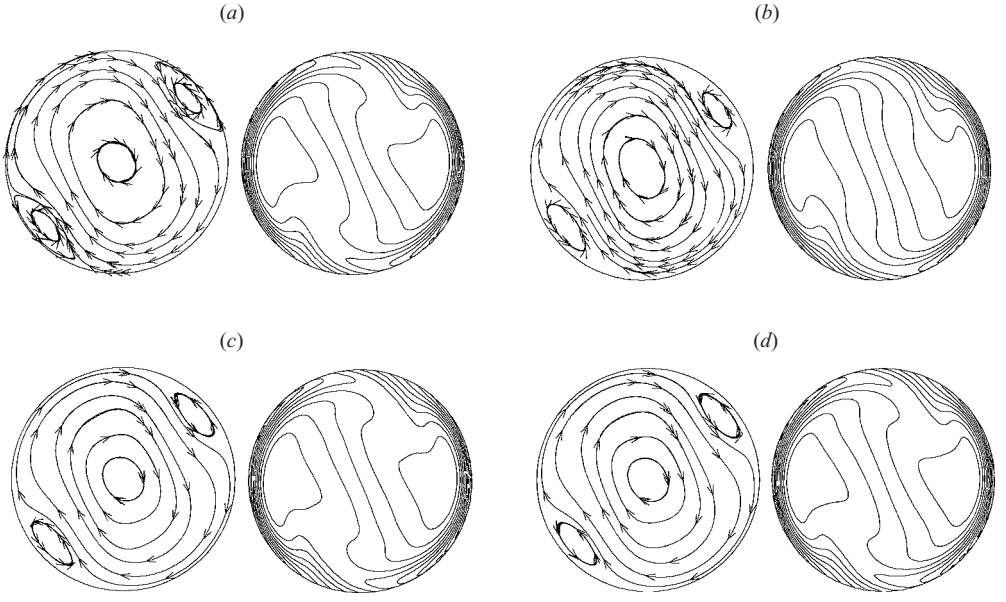

FIGURE 3. Comparison of the streamline (left) and isotherm (right) patterns reconstructed using POD modes with the numerical simulations at $\tau = 1.17$ for $Ra_\Omega = 10^2$. (*a*) DNS snapshot, (*b*) 5 modes, (*c*) 10 modes, (*d*) 15 modes.

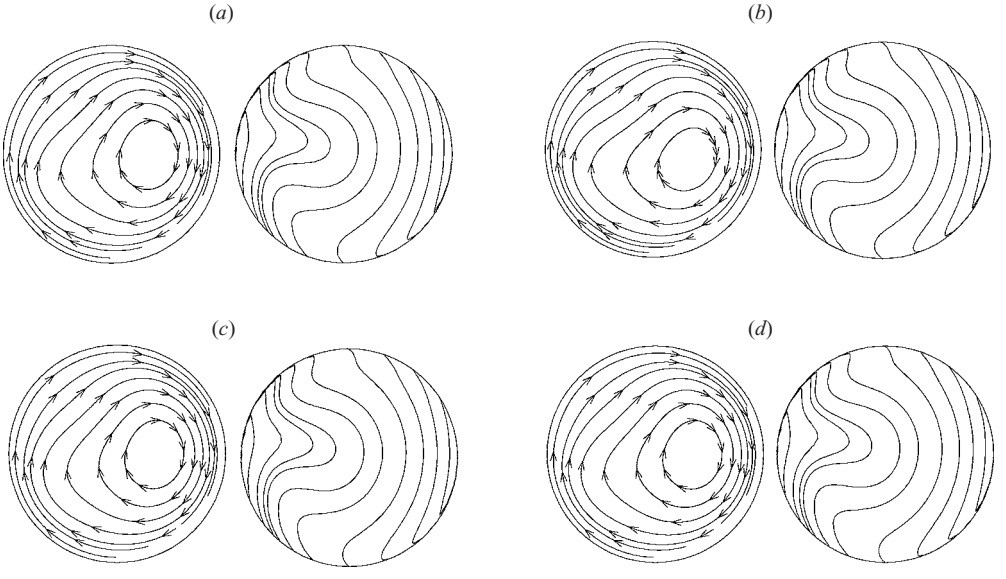

FIGURE 4. Comparison of the streamline (left) and isotherm (right) patterns reconstructed using POD modes with the numerical simulations at $\tau = 1.0019$ for $Ra_\Omega = 10^4$. (*a*) DNS snapshot, (*b*) 1 mode, (*c*) 2 modes, (*d*) 4 modes.

the complexity of the flow structure increases as indicated by the DNS snapshot in figure 5. The details of the flow structure are captured well by an eight-mode POD expansion. The error norms are reduced to less than 5 % for 10 modes as seen from table 2. Similar results for reconstruction were found for other values of Ra_Ω.

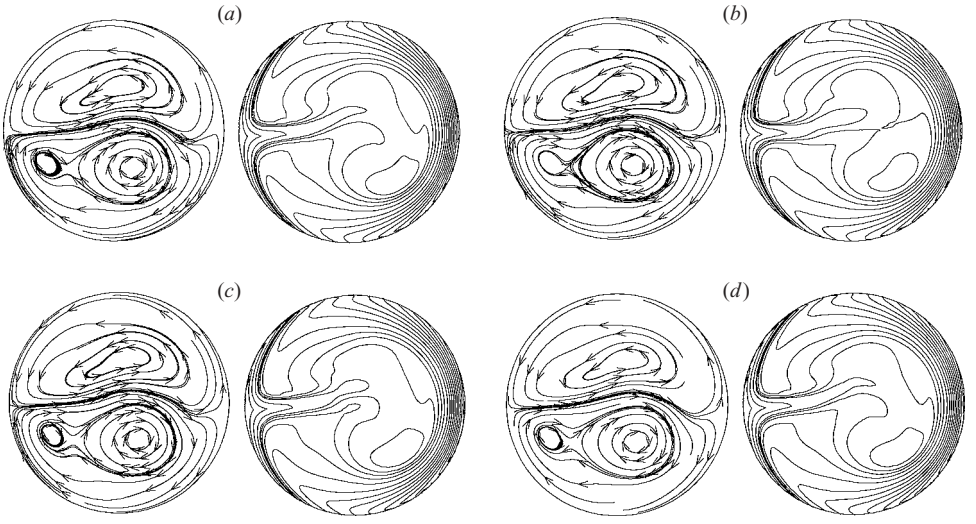

FIGURE 5. Comparison of the streamline (left) and isotherm (right) patterns reconstruction using POD modes with the numerical simulations at $\tau = 1.6473$ for $Ra_\Omega = 10^6$. (*a*) DNS snapshot, (*b*) 2 modes, (*c*) 4 modes, (*d*) 8 modes.

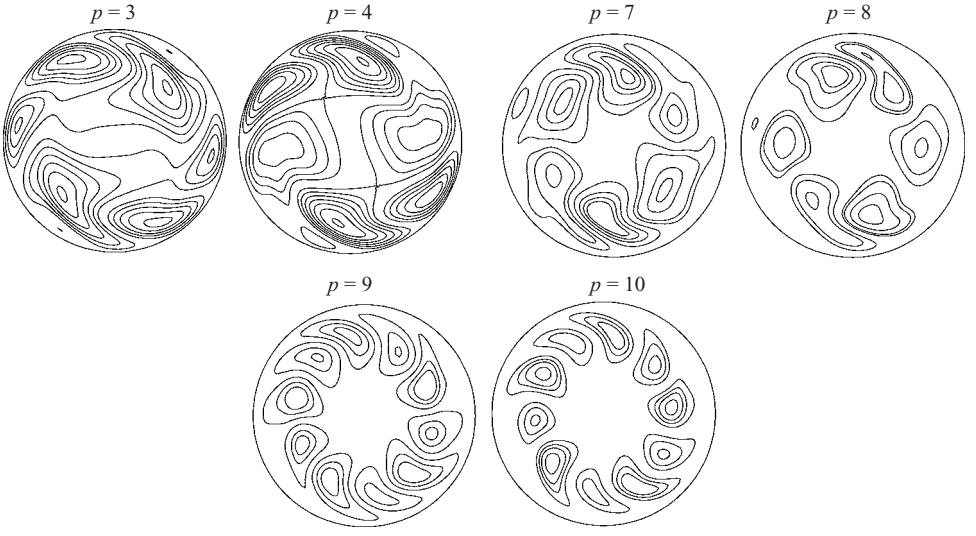

FIGURE 6. The spatial structures of the contributions of pairs of POD modes having equal eigenvalues to the temperature field at $\tau = 2.575$ at $Ra_\Omega = 10^3$.

Returning to the eigenvalue spectra in figure 2, it is observed that for $Ra_\Omega = 10^3$ (figure 2*b*), a number of eigenvalues are degenerate, i.e. occur in pairs. The eigenvalues for modes (3, 4), (7, 8) and (9, 10) are some of the more energetic degenerate pairs. The degeneracy of the eigenspectrum has its roots in the symmetries of the flow solution as demonstrated in Aubry, Guyonnet & Lima (1992), Aubry & Lian (1993), Aubry & Lima (1995) and Aubry (1991). To observe such symmetries, time histories of the temporal coefficients of a degenerate pair of modes $(a^{(q)}(t),\ a^{(q+1)}(t))$ and the contributions of the individual modes of the selected degenerate pair to the flow field at an instant are compared. Figure 6 shows the spatial structure of the individual contributions

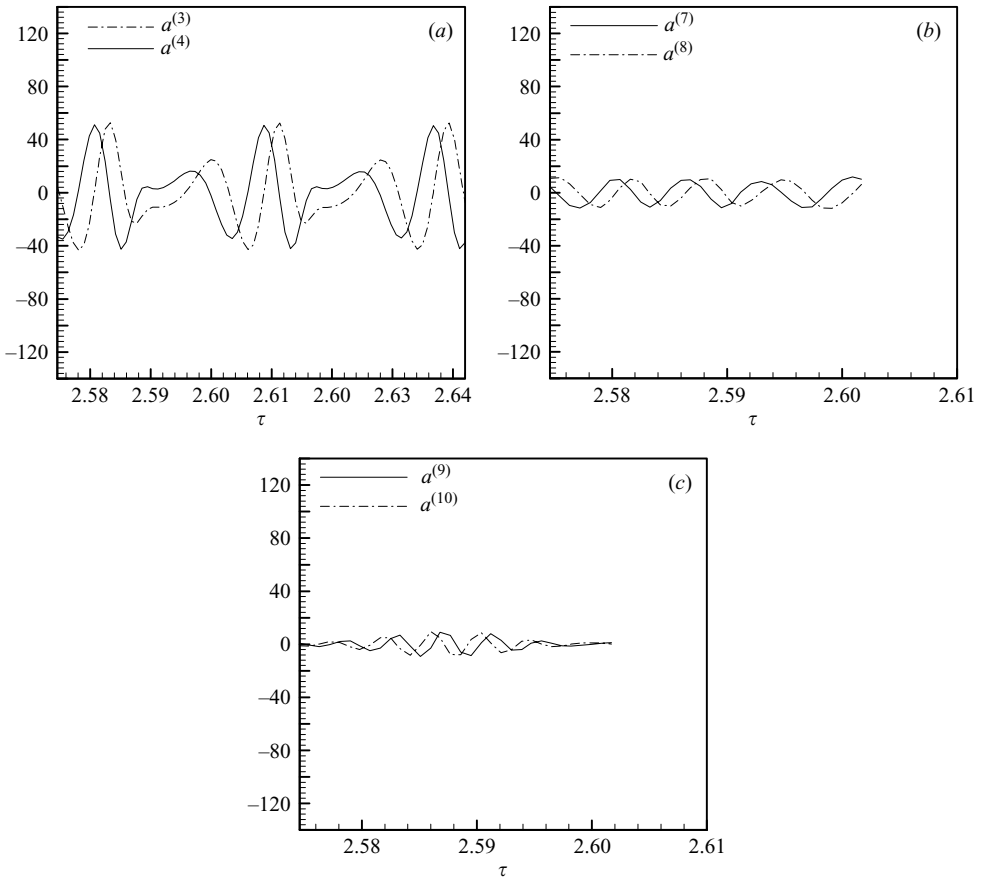

FIGURE 7. The time evolution of temporal coefficients of degenerate pairs of modes at $Ra_\Omega = 10^3$.

of POD modes having equal eigenvalues to the thermal field at $\tau = 2.575$. It is observed that the contour patterns are shifted in the circumferential direction. This clearly suggests a translational shift in the circumferential direction in the spatial structure of the degenerate pair of modes. Some of the structures experience some distortion along with this shift. The distortion is expected due to nonlinear convective interactions and diffusive effects. Figure 7 compares the time histories of the coefficients for several degenerate pairs of modes. It is readily seen that the pair of coefficients $a^{(3)}$ and $a^{(4)}$, as well as other pairs, are almost identical except for a phase shift in time. In order to highlight the spatial shift in the circumferential direction of the structures of the eigenfunctions $\boldsymbol{\phi}^{(3)}$ and $\boldsymbol{\phi}^{(4)}$, the components $\phi_3^{(3)}$ and $\phi_3^{(4)}$ are plotted in figure 8 as functions of the angular coordinate α (positive in the counterclockwise sense) in the rotating frame at a fixed radius of 0.85. It is readily observed that the spatial structures of $\phi_3^{(3)}$ and $\phi_3^{(4)}$ exhibit a translational symmetry in the circumferential direction. While mode 3 is shifted in the counterclockwise direction relative to mode 4 in space, mode 3 also leads mode 4 in time (figure 7). This clearly suggests that the degenerate pair (3, 4) represents a propagating structure or a travelling wave in the clockwise direction with the flow. Rempfer & Fasel (1994) also exploited the space–time symmetry of a propagating flow structure to demonstrate the existence of travelling waves in a transitional boundary-layer flow over a flat plate. Similar space–time symmetries are

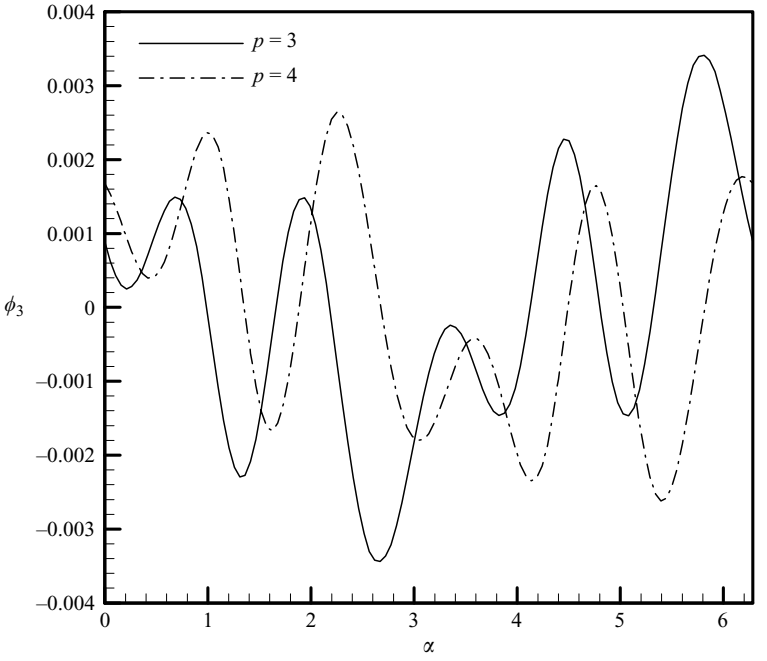

FIGURE 8. Variation of the temperature eigenfunctions ϕ_3 in the circumferential direction at a radius of 0.85 for the degenerate pair (3, 4).

exhibited by other degenerate pairs. The deviations from the perfect translational symmetry in space and time can be attributed to the fact that the propagating structures represent modulated travelling waves. Thus it can be argued that at $Ra_\Omega = 10^3$ the flow exhibits travelling waves propagating in the circumferential direction. In the numerical study of HS, it was argued on the basis of spatial flow structure that at $Ra_\Omega = 10^3$, the centrifugal buoyancy force is too weak to exert any significant influence on the flow. To confirm this, numerical simulations were performed by neglecting the centrifugal buoyancy term in (2) for different values of Ra_Ω in the range $10^3 < Ra_\Omega < 10^4$. Figure 9 compares the time history of the v velocity at $(-0.72, 0)$ obtained through numerical solution of the full equations (1)–(3), to the time history obtained by neglecting the centrifugal buoyancy term at $Ra_\Omega = 1.2 \times 10^3$. It is readily verified that for such a low value of Ra_Ω, the centrifugal effects are insignificant. Thus the travelling waves found are generated due to the combined action of gravity, the fluid inertia and the viscous forces. Such waves have not been reported in the earlier studies of Hamady *et al.* (1994) and Ker & Lin (1996) on rotating rectangular containers.

For the case of a traveling wave, as pointed out by Aubry *et al.* (1992), the space–time shifts in the POD eigenfunctions and the temporal coefficients for a given degenerate pair of modes can be exploited to determine the wave speed (phase speed of the wave). For a uniformly traveling one-dimensional wave, the phase speed of the wave can be determined by the ratio of the spatial and the temporal shifts observed in the eigenfunctions and the temporal coefficients of the degenerate pair of modes (Aubry *et al.* (1992)). The situation is somewhat complex for a multi-dimensional scenario with the direction of wave propagation not necessarily coinciding with the coordinate directions. Thus different spatial shifts in the eigenfunctions would be recorded in different directions. In the present context, it has been shown that

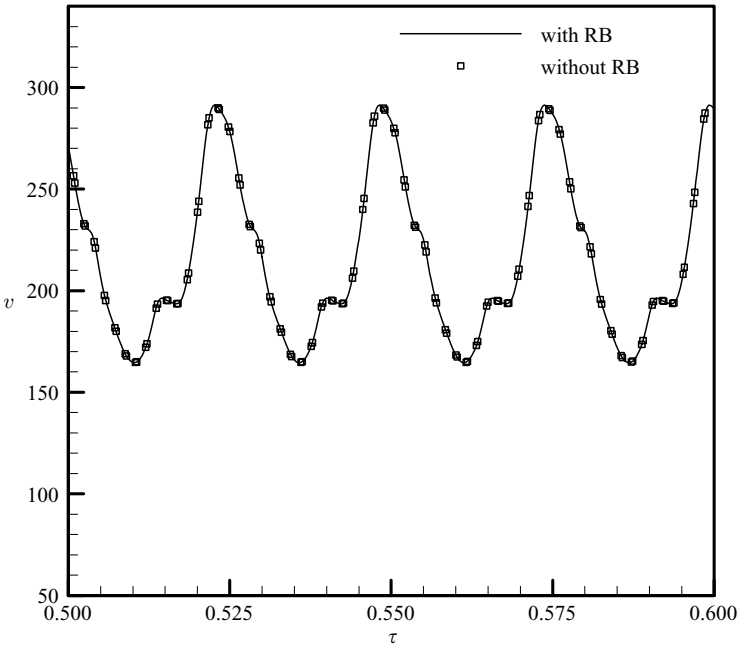

FIGURE 9. Comparison of time histories of v velocity at $(-0.72, 0)$ obtained by neglecting the rotational buoyancy (RB) with the data obtained from the full set of equations at $Ra_\Omega = 1.2 \times 10^3$.

the waves are propagating pre-dominantly in the circumferential direction in the clockwise sense at $Ra_\Omega = 10^3$. The presence of such waves is also confirmed, in a similar manner, for neighbouring values of $Ra_\Omega = 1.2 \times 10^3$, 1.5×10^3, 1.7×10^3 and 1.9×10^3. The major concern in estimating the circumferential wave speeds is the fact that the translational shifts in the temporal coefficients and the eigenfunctions for a degenerate pair are not uniform in time and space respectively. Therefore, estimates of the average circumferential wave speed ($\bar{c}_\alpha$) at a particular radius of 0.85 are made on the basis of the average translational shifts (both in space and time) in the structure of the degenerate pair of modes. Table 3 compares these circumferential wave speeds to the time-mean spatially averaged circumferential flow velocity ($\bar{u}_\alpha$) at the same radius in order to obtain some insight into the wave properties. For all the values of Ra_Ω, the circumferential waves are observed to propagate in the clockwise direction which is also the general direction of the flow velocities. It is interesting to observe that the ratio $\bar{c}_\alpha/\bar{u}_\alpha$ lies in the range 0.47–0.8.

For $Ra_\Omega = 10^6$, the flow exhibits quasi-periodicity as reported in the computational study of HS. At this Ra_Ω, the POD eigenvalue spectrum in figure 2(*e*) again hints at the existence of propagating structures or travelling waves in the form of degenerate eigenvalues. The eigenvalues for modes 5 and 6 and modes 7 and 8 are nearly identical. The spatial structure of the contribution of these modes to the fluctuating thermal field at an instant is shown in figure 10. It can be observed that the structures represented by the 5th and 6th modes propagate along with the flow (the pattern shown in figure 5) on either side of the horizontal diameter. Simultaneously, a shift in the spatial structures in the circumferential direction near the hot end (left end) of the horizontal diameter is also observed. This hints that these waves may have originated in the boundary layers near the hot end and move with the fluid. Similar observations

Ra_{Ω}	Degenerate pair $(q,\ q+1)$	Wave speed $\bar{c}_{\alpha}$	Fluid velocity $\bar{u}_{\alpha}$	$\frac{\bar{c}_{\alpha}}{\bar{u}_{\alpha}}$
	(3, 4)	124.14		0.807
1.0×10^3			153.84	
	(7, 8)	119.42		0.774
	(3, 4)	87.94		0.516
1.2×10^3			170.48	
	(5, 6)	1.14		0.476
	(3, 4)	101.73		0.537
1.5×10^3			189.50	
	(5, 6)	7.03		0.512
	(3, 4)	8.76		0.495
1.7×10^3			199.49	
	(5, 6)	9.12		0.497
	(3, 4)	136.89		0.659
1.9×10^3			207.85	
	(5, 6)	8.52		0.474

TABLE 3. Average wave speeds (clockwise circumferential direction) at a radius of 0.85 for different propagating structures at different Ra_{Ω}. Wave speeds are compared with the time-mean, spatially averaged circumferential flow velocity (also clockwise) at a radius of 0.85.

can be made for the 7th and 8th modes. In order to confirm the propagation of waves along the horizontal diameter ($y = 0$), the structure of the temporal coefficients and the eigenfunctions ϕ_3 for the degenerate pairs (5, 6) and (7, 8) are compared in figure 11(*a*) and figure 11(*b*) respectively. The space–time translational shifts are again observed, providing clear evidence of the presence of propagating or travelling waves. Modes 5 and 7 are shifted towards the right in both the spatial and the temporal domains with respect to mode 6 and 8 respectively. This is clear evidence of the wave propagating along $y = 0$ in the positive x-direction (from the hot end towards the cold end) of the rotating enclosure. From figure 11(*b*), it can be observed that the spatial translational shifts are large near the hot end ($x = -1$) and progressively decrease towards the cold end ($x = 1$). This suggests that wave speeds are much higher near the hot end and progressively decrease as the wave propagates towards the cold end. At $Ra_{\Omega} = 10^6$, the flow is primarily driven by centrifugal or rotational buoyancy force with effects of gravity becoming quite insignificant. Thus, it is the interaction of viscous, centrifugal buoyancy and the inertia forces that is responsible for the waves at this Ra_{Ω}.

3. Low-dimensional models

In this section the construction and performance of low-dimensional models based on the empirical eigenfunctions obtained during the course of the POD analysis is discussed. In § 3.1 issues regarding construction of these models are addressed. In § 3.2 the validation of the low-dimensional models is presented. Finally in § 3.3 their performance for parameters different from the ones from which they were constructed is examined.

3.1. *Construction of POD–Galerkin models*

The low-dimensional model refers to the system of ODEs governing the evolution of temporal coefficients in (9). The standard procedure for obtaining such a system of

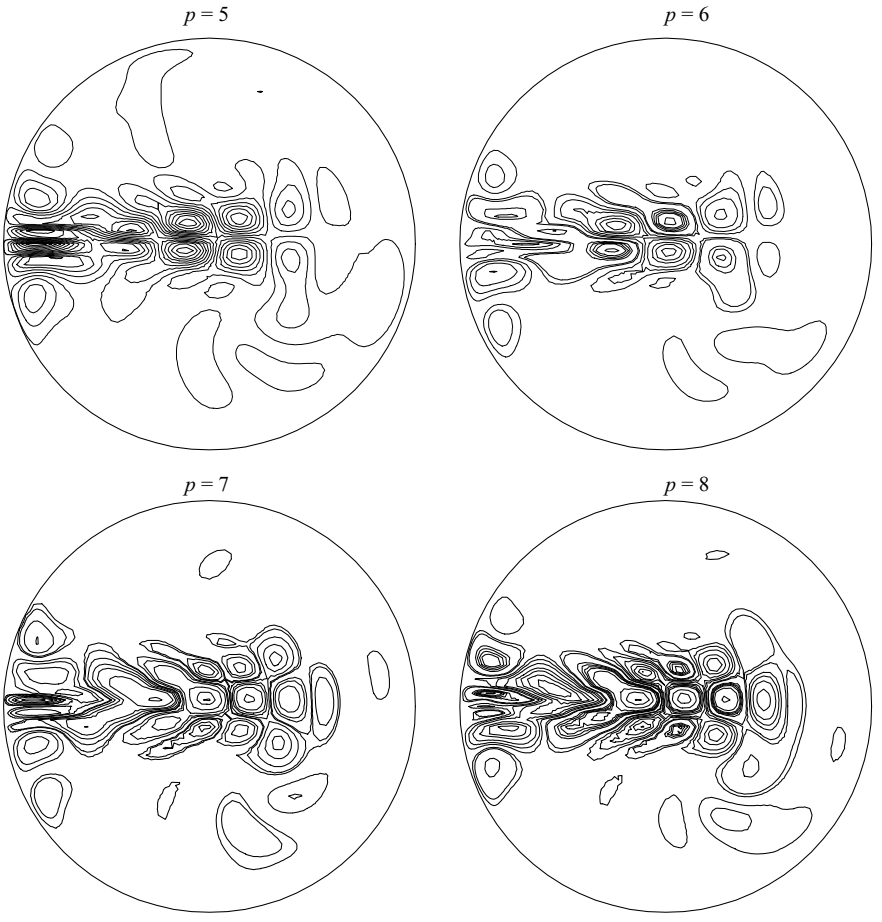

FIGURE 10. The spatial structures of the contributions of pairs of POD modes having equal eigenvalues to the temperature field at $\tau = 1.605$ at $Ra_\Omega = 10^6$.

ODEs is Galerkin projection. In this procedure the governing equations for the flow field are projected onto the individual POD modes or basis functions.

As mentioned by Rempfer (2000), the Galerkin projection requires the basis functions to fulfil certain conditions. In the context of a Galerkin procedure for an incompressible flow, the basis functions should be capable of representing all solenoidal velocity fields that satisfy the boundary conditions. In this regard, the POD eigenfunctions provide an excellent choice of basis functions as any property or boundary condition of the flow, which is expressed via linear homogenous equations, is passed on to these individual basis functions. The incompressibility constraint, no-slip boundary conditions and periodic boundary conditions are some examples of such properties. In the present study, since the POD eigenfunctions have been obtained for the fluctuating component of the flow field, the homogeneous boundary conditions for the fluctuating or unsteady flow ($u' = v' = \theta' = 0$) are passed on to each eigenfunction, making it vanish at the domain boundary. Since each individual eigenfunction is capable of satisfying the boundary condition no compatibility constraints are imposed on these basis functions.

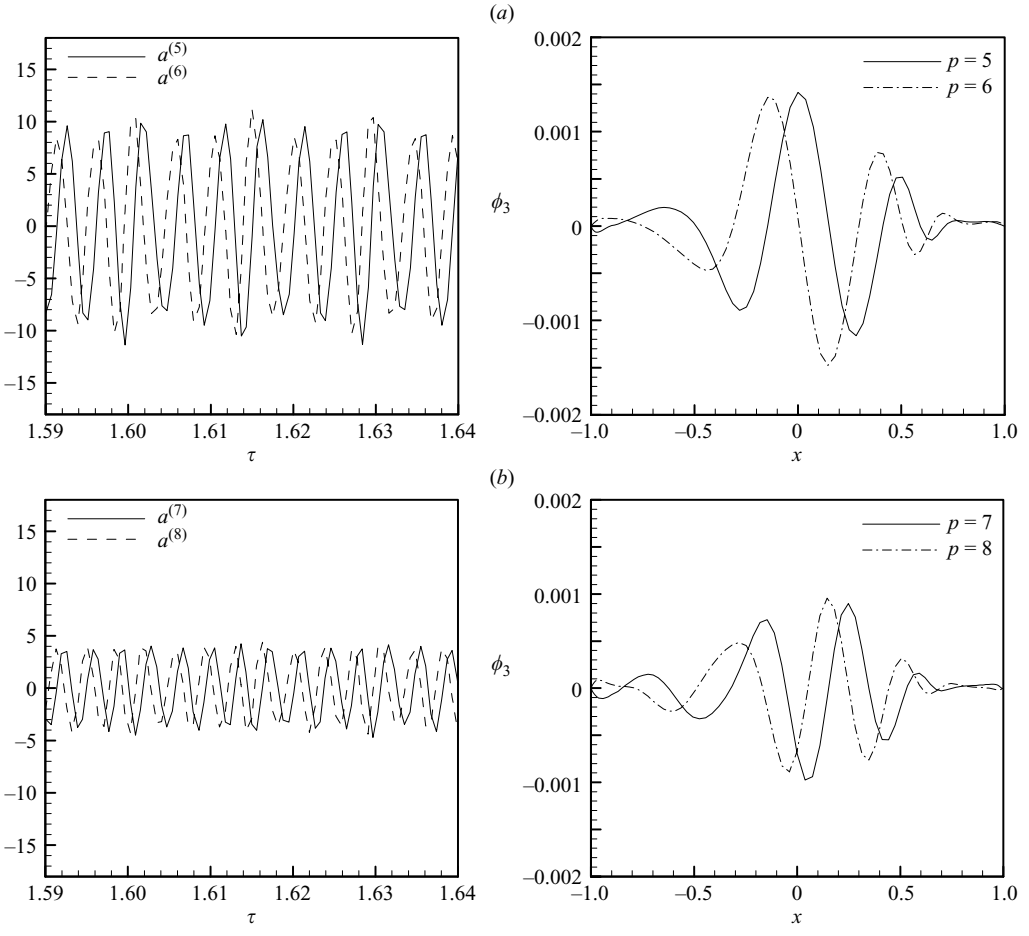

FIGURE 11. Comparison of the evolution of the temporal coefficients and the structure of temperature eigenfunctions at $y = 0$ for the degenerate pair of modes (*a*) (5, 6) and (*b*) (7, 8) at $Ra_\Omega = 10^6$.

The Galerkin projection leads to an infinite system of ODEs for the temporal modal coefficients of the form

$$\frac{\mathrm{d}a^{(p)}}{\mathrm{d}\tau} = F^{(p)}\left(a^{(1)}, a^{(2)}, \ldots, \tau\right), \qquad p = 1, 2, \ldots, \infty. \tag{13}$$

The infinite system in (13) is truncated at some level of the quantum number p to yield the low-dimensional model, with the hope that the effect of truncation on the system dynamics is not significant. The truncation of the infinite system in (13) will be elaborated when the validation and performance assessment of the low-dimensional model is presented.

In order to carry out the Galerkin projection for the present problem the governing equations for the fluctuating or unsteady flow have been obtained. Following the Reynolds decomposition approach, the instantaneous flow variables in equations (1)–(3) are considered to be compresed of a steady or mean part and a fluctuating component.

Symbolically this is expressed as

$$\left.\begin{aligned} v_i(x,y,t) &= U_{mi}(x,y) + u_i'(x,y,t),\\ \theta(x,y,t) &= \Theta_m(x,y) + \theta'(x,y,t),\\ p(x,y,t) &= P_m(x,y) + p'(x,y,t). \end{aligned}\right\} \tag{14}$$

Substituting in equations (1)–(3) and time averaging the terms leads to equations governing the mean flow. The mean flow equations are then subtracted from (1)–(3) to yield the equations for the fluctuations. The governing equations for the fluctuating flow field in Cartesian tensor notation are

$$\frac{\partial u_j'}{\partial x_j} = 0, \tag{15}$$

$$\begin{aligned} \frac{\partial u_i'}{\partial \tau} = {} & Ra_g Pr\big[\big\{(\Theta_m+\theta')\sin\left(Ta^{1/2}Pr\tau\right) - \left\langle\theta'\sin\left(Ta^{1/2}Pr\tau\right)\right\rangle\big\}\delta_{i1}\\ & + \big\{(\Theta_m+\theta')\cos\left(Ta^{1/2}Pr\tau\right) - \left\langle\theta'\cos\left(Ta^{1/2}Pr\tau\right)\right\rangle\big\}\delta_{i2}\big] - 2Ta^{1/2}Pr\, e_{i3j}u'_j\\ & - Ra_\Omega Pr\theta' x_i - \frac{\partial p'}{\partial x_i} - u'_j\frac{\partial U_{mi}}{\partial x_j} - U_{mj}\frac{\partial u_i'}{\partial x_j} - u'_j\frac{\partial u_i'}{\partial x_j} + \frac{\partial\langle u_i'u_j'\rangle}{\partial x_j} + Pr\frac{\partial^2 u_i'}{\partial x_j\partial x_j}, \end{aligned} \tag{16}$$

$$\frac{\partial\theta'}{\partial\tau} = -u'_j\frac{\partial\Theta_m}{\partial x_j} - U_{mj}\frac{\partial\theta'}{\partial x_j} - u'_j\frac{\partial\theta'}{\partial x_j} + \frac{\partial\langle\theta'u_j'\rangle}{\partial x_j} + \frac{\partial^2\theta'}{\partial x_j\partial x_j}. \tag{17}$$

In equations (15)–(17), $(i, j) \in [1, 2]$.

These equations are similar to the ones employed in the work of Podvin & Le Quéré, (2001) except for the extra terms due to the rotating frame of reference. While the Coriolis and centrifugal terms do not pose any difficulty, the periodic forcing by the rotating gravity vector gives rise to two terms: $\langle\theta'\sin(Ta^{1/2}Pr\tau)\rangle$ and $\langle\theta'\cos(Ta^{1/2}Pr\tau)\rangle$. These terms represent the correlation between the fluctuating thermal field and the components of a unit vector indicating the instantaneous direction of the rotating gravity vector. For a turbulent motion the correlation between a random fluctuating thermal field and a completely organized sinusoidal signal is expected to be very small and therefore can be neglected. However for a non-turbulent flow, which is the subject of the present work, significant correlation may exist. Therefore these terms are retained in the equations for the fluctuating flow field. The information on mean flow is directly available from the data ensemble. Thus the mean flow field (U_{m1}, U_{m2}, Θ_m) is regarded as a known input in equations (16)–(17) and in the subsequent low-dimensional model.

The POD expansions for the fluctuating variables are substituted in (16)–(17) and then the Galerkin projection is carried out to obtain the system of ODEs involving the temporal coefficients. For notational convenience, the mean and the fluctuating thermal field are denoted as U_{m3} and u_3'. The various correlations, i.e. $\langle u_i'u_j'\rangle$, needed to close the system of equations have been expressed in terms of the POD modes in the following manner:

$$\langle u_i'u_j'\rangle = \sum\sum\langle a^{(r)}a^{(s)}\rangle\phi_i^{(r)}\phi_j^{(s)} = \sum_r \lambda^{(r)}\phi_i^{(r)}\phi_j^{(r)}, \quad i = 1,\ldots,3,\ j = 1,2. \tag{18}$$

The correlations of type $\langle\theta'\sin(Ta^{1/2}Pr\tau)\rangle$ or $\langle u_3'\sin(Ta^{1/2}Pr\tau)\rangle$ can be expressed as

$$\left\langle u_3'\sin\left(Ta^{1/2}Pr\tau\right)\right\rangle = \sum_r\left\langle a^{(r)}\sin\left(Ta^{1/2}Pr\tau\right)\right\rangle\phi_3^{(r)}. \tag{19}$$

If the expression in (19) is employed, the low-dimensional model for the temporal coefficients would not be closed. This closure problem has arisen from the specific

nature of the problem being studied and has not been tackled in earlier works. One way of circumventing this closure problem is to utilize the computational data for θ' directly to estimate this correlation without using the POD eigenfunctions. However, this goes against the very spirit of a low-dimensional model, the primary purpose of which is to capture the dynamics of the flow in terms of the evolution of some dominant structures in the flow. Therefore the various terms that constitute a low-dimensional model must be built or evaluated on the basis of these dominant structures. In an attempt to incorporate the above considerations and to simultaneously overcome the closure problem, the temporal coefficients $a^{(r)}$ on the right-hand side of (19) are taken to be the DNS coefficients obtained by projecting the modes $\boldsymbol{\phi}^{(r)}$ onto the data ensemble.

The fluctuating pressure field p' does not make any contribution to the low-dimensional model. This can be readily verified, since the contribution of the pressure field via Galerkin projection given as

$$\int_D \phi_j^{(p)} \frac{\partial p'}{\partial x_j} \, \mathrm{d}A,$$

is identically zero due to the fact that the eigenfunction is solenoidal and it vanishes at the boundary of the flow domain.

Finally, the Galerkin projection yields the following system of equations:

$$\frac{\mathrm{d}a^{(p)}}{\mathrm{d}t} = L_{pr}(\tau)a^{(r)} - Q_{prs}a^{(r)}a^{(s)} + F_p(\tau), \quad p, r, s = 1, 2, \ldots, \infty. \tag{20}$$

Truncating the above system (20) by retaining the first N modes yields an N-dimensional model. The definitions of the various coefficients and terms in (20) are given in the Appendix. The term $F_p(\tau)$ in (20) is an harmonic forcing function associated with the rotating gravity vector as defined in the Appendix. Thus the system in (20) has the character of a nonlinear forced oscillator.

3.2. *Validation and performance of the POD–Galerkin models*

In order to validate and assess the performance of the low-dimensional models, the five values of Ra_Ω which have been analysed using POD are considered. Comparison of the temporal coefficients $a^{(p)}(\tau)$ obtained from the low-dimensional model with those obtained directly from the computational data is taken to be the criterion for valid and accurate solutions of these low-dimensional models. The truncation of the POD–Galerkin models is guided by the convergence characteristics of the POD-mode-based reconstructions as discussed in § 2.3.

Another issue related to the truncation of the POD–Galerkin models is the effect of neglected modes on the long-term behaviour of the low-dimensional model. It is known that if sufficient modes are not included then the required amount of energy of the system is not dissipated and accumulates in the first few modes or the large scales of the motion. Thus in the large time limit, the system would become unstable. In the present study enough modes have been chosen to ensure not only the stability of the low-dimensional system but also the ability to accurately reproduce the system dynamics.

For $Ra_\Omega = 10^2$, a five-dimensional model is found to be sufficient to carry out integration of the low-dimensional model for very long times (~ 400 dimensionless units) without any blowing up of the solution. The initial condition for the low-dimensional model is taken to be the values of the temporal coefficients obtained from the computational data at the appropriate time instant.

At this stage, it is worth discussing the role of the scaling factor γ in the definition of the inner product. In the work of Podvin & Le Quéré (2001), a value of unity for the scaling factor works reasonably well and a value based on the criterion given in (7), which equals 4.68, provides only slightly better performance of the low-dimensional model. However, when a value of unity was tried in the present study, the eigenfunctions failed to capture the dominant structures accurately. More significantly, the low-dimensional model experienced rapid divergence leading to a solution blow-up in a very short interval of time. This is not surprising when one considers the fact that the values of γ obtained using (7) for the different cases of Ra_Ω varied between 10^5 and 10^7. Therefore, it can be concluded that in general for flows involving transport of some scalar, in addition to the velocity components, it is important that the value of the scaling factor γ be obtained by using (7).

Before discussing the performance of the low-dimensional models, the effect of retaining the correlations of type $\langle\theta' \sin(Ta^{1/2}Pr\tau)\rangle$ in the fluctuation equations is examined. Figure 12 shows the time evolution of the coefficients of the leading five POD modes obtained from a 10-mode truncated low-dimensional model (referred to as M10) with and without the correlation term D_p (the Appendix). The values of the coefficients obtained through projection of the modes onto the computational data are also shown. During some time intervals the effect of neglecting D_p is barely noticeable. However, there is a slight loss of accuracy during the other portions of the time history but the qualitative aspects are preserved. Since estimation of the term D_p requires a large amount of data, retaining it is justified only if the data are available and quantitative accuracy is an important issue. For the present study, the term D_p is retained for all the cases of Ra_Ω.

Figures 13–16 depict the performance of the low-dimensional models for $Ra_\Omega = 10^2$, 10^4 and 10^6 respectively. At $Ra_\Omega = 10^2$ (figure 13), a twenty-dimensional model captures the temporal evolution of the modal coefficients quite faithfully. Slight deviations are observed in the trajectories of 10th and 15th modes. However, these modes contribute very little to the total energy and therefore the deviations are not significant. The time period of the various temporal coefficients is found to be 0.088 dimensionless units which matches the period of rotation of the gravity vector (0.0885) at this Ra_Ω. Therefore, the phenomenon of frequency-locking is captured quite well. Another feature that can be observed is that while the more energetic structures have a simple periodic structure in time, the less energetic structures (10th and 15th modes) have a greater amount of complexity in their temporal structure.

As shown in the study of HS, the phenomenon of frequency-locking persists for $Ra_\Omega \leqslant 10^5$. This is reflected in the solution of the low-dimensional models for $Ra_\Omega = 10^2$ and 10^4(figures 13 and 14). At $Ra_\Omega = 10^4$, an 8-mode model captures the dynamics faithfully. The time period of the various temporal coefficients is found to be 0.00886 dimensionless units. This agrees quite well with the period of the rotating gravity vector given as 0.00885. Similar results are obtained for other cases of frequency-locked motion at $Ra_\Omega = 10^3$ and $Ra_\Omega = 10^5$. As mentioned in § 1.3, for $Ra_\Omega \leqslant 10^5$ the fluctuation levels of the flow decrease with increase in Ra_Ω. This feature is also readily captured by the low-dimensional models. The decreasing complexity in the flow structure, as confirmed by the POD analysis in § 2.3, is also confirmed by the fact that the number of modes needed to accurately model the system dynamics decreases from 20 to 8 with increase in Ra_Ω from 10^2 to 10^4. In fact, for the nearly steady flow at $Ra_\Omega = 10^5$, a 4-mode model captures the temporal dynamics faithfully.

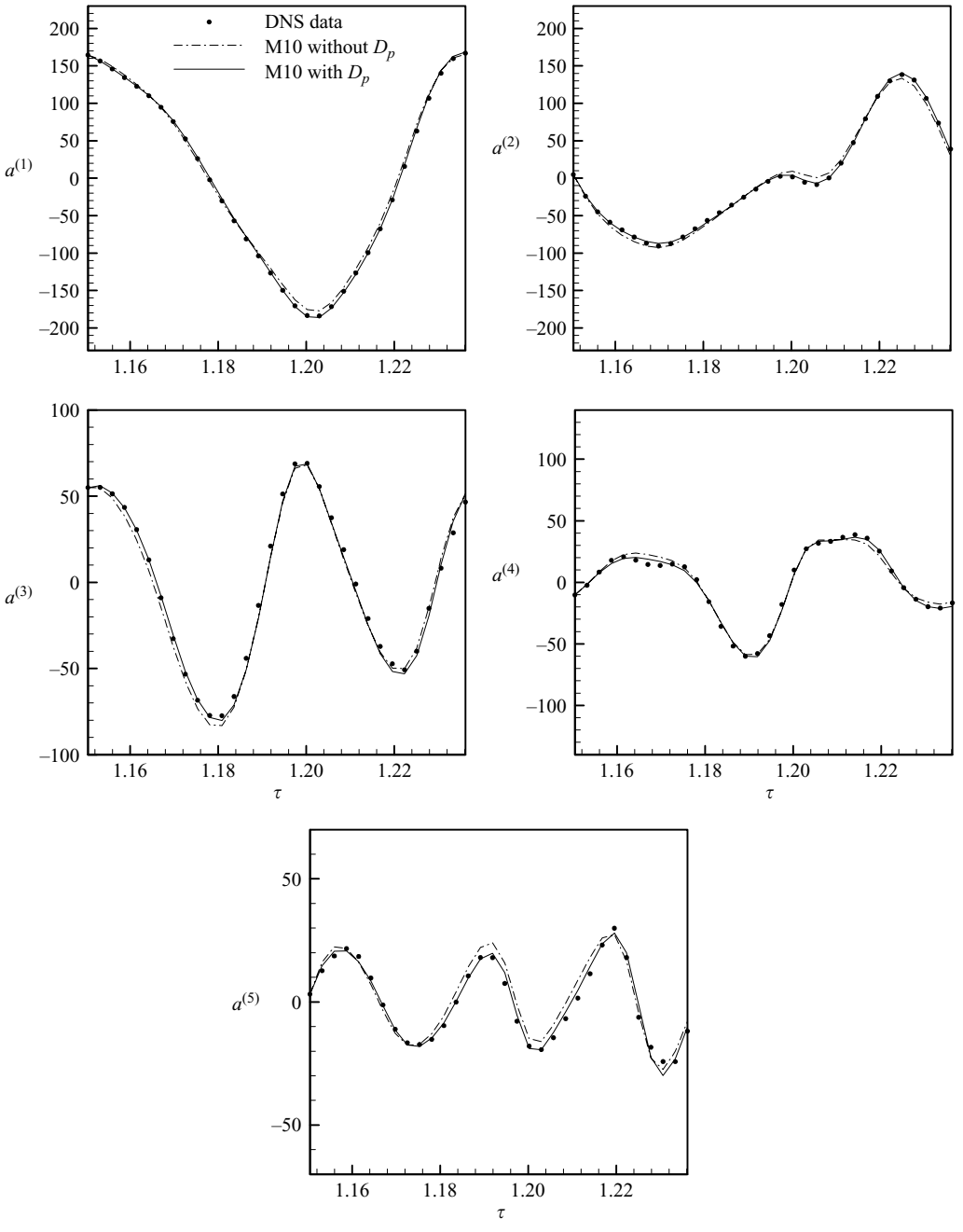

FIGURE 12. Comparison of time histories of the temporal modal coefficients obtained from a ten-dimensional model (with and without the term D_p) and by projecting the modes onto the computational data for $Ra_\Omega = 10^2$.

For $Ra_\Omega = 10^6$, the flow is quasi-periodic and the level of fluctuation begins to rise again. Figures 15 and 16 depict the trajectories of the temporal coefficients obtained from a ten-dimensional model. The model reproduces the dynamics quite nicely as the trajectories follow their DNS paths.

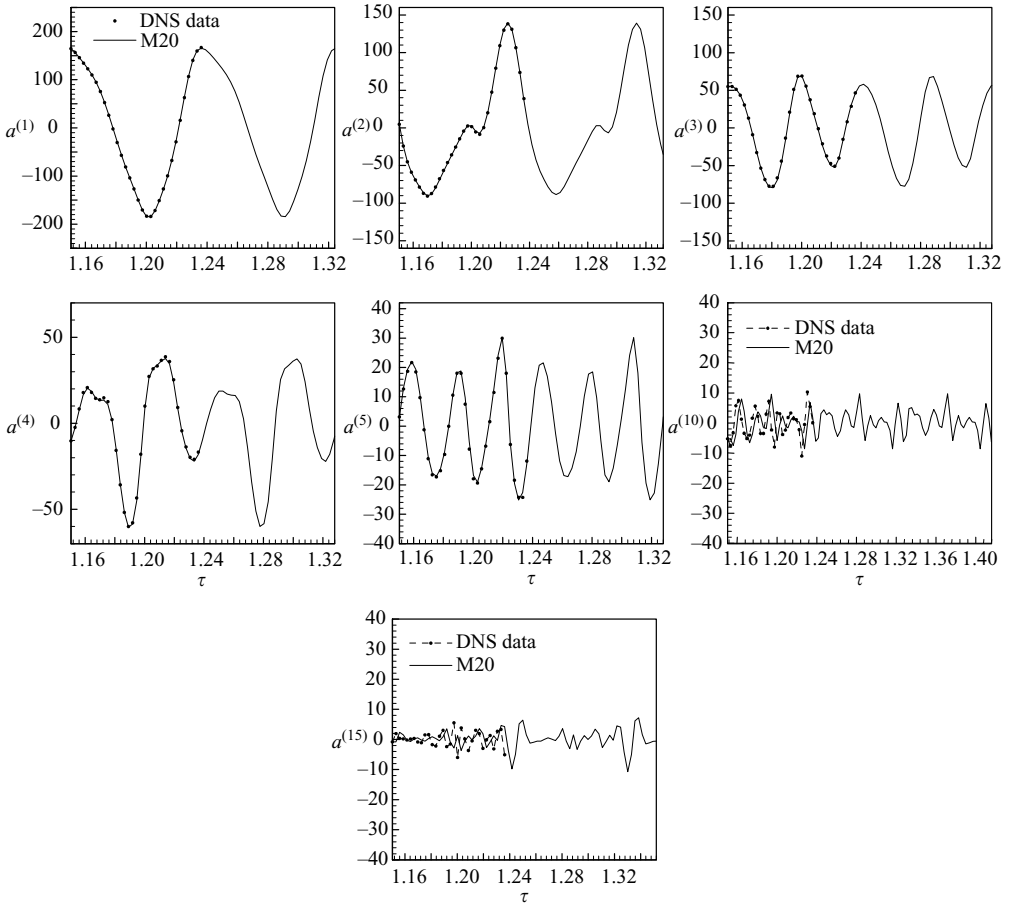

FIGURE 13. Comparison of time histories of the temporal modal coefficients obtained from a twenty-dimensional model and the computational data for $Ra_\Omega = 10^2$.

In order to check for any build up of errors in the solution of the low-dimensional models, the time integrations were carried out for as long as several hundred cycles of the gravity vector. The models did not exhibit any blow-up or even slow divergence.

One of the criticisms of the low-dimensional modelling approach is the requirement of a large amount of data. This can be partially overcome if the low-dimensional models constructed from data available for a limited set of the parameters also reproduce the dynamics reasonably accurately over a range of parameters different from the ones from which they were constructed. This is potentially attractive, but as pointed out by Rempfer (2000), the success of a low-dimensional model in such a situation is not guaranteed. Further, the initial velocity field employed to provide the initial condition for the low-dimensional model must also be a part of the original data ensemble. Thus the performance of a low-dimensional model for a set of system parameters different from the one from which it was constructed from is worth examining. In some recent studies, hybrid models constructed from data spanning a range of parameters have been shown to perform reasonably well. Most of these studies involve isothermal flows rather than flows with heat transfer.

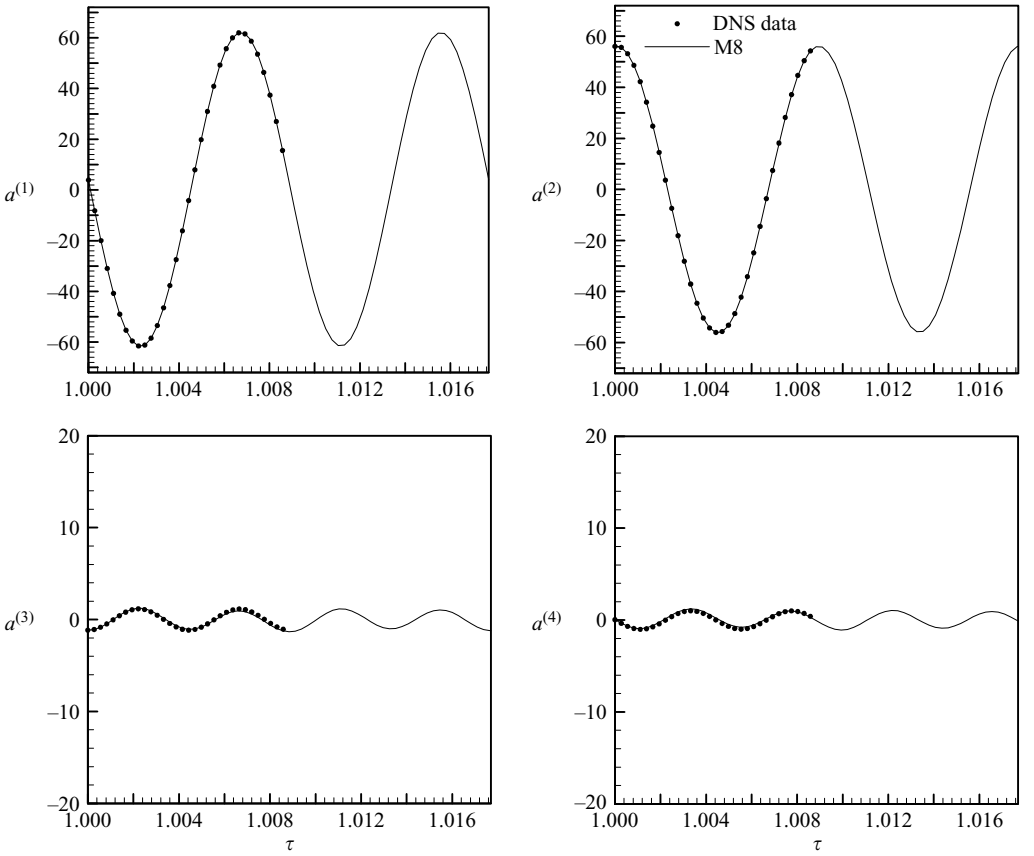

FIGURE 14. Comparison of time histories of the temporal modal coefficients obtained from an eight-dimensional model and the computational data for $Ra_\Omega = 10^4$.

3.3. *Performance of the hybrid models*

The simplest strategy to construct a hybrid model is to combine the snapshots obtained for different sets of parameters spanning the range of interest into a single data ensemble. The data ensemble comprising this mix of snapshots is then decomposed into modes, which could then be utilized to construct the low-dimensional model. An other way is to decompose the sets of snapshots for different parameters into modes and then perform a Gram–Schmidt orthogonalization on the different sets of modes to yield a combined orthogonal set of modes. In this work we adopt the former strategy, as adopted earlier by Ma & Karniadakis (2001). A set of 32 snapshots from each numerical database at $Ra_\Omega = 10^2$ and $Ra_\Omega = 10^3$ is taken and a single data ensemble is formed comprising 64 snaps. This data ensemble is decomposed into modes using the method of snapshots as discussed in § 2.2. A convergence study as in § 2.3 is carried out for modal reconstruction of the mixed ensemble. It is found that 35 modes are needed for the error norms to reduce to around 5 %. Thus the model is constructed by truncating the POD–Galerkin model using the first 50 modes.

In the construction of the hybrid low-dimensional model there are two principal concerns. The low-dimensional model requires knowledge of mean flow field in the estimation of the term L^M_{pr}, the Appendix defined in. However, since the hybrid model is targetted to perform at a parameter value different from those correponding to

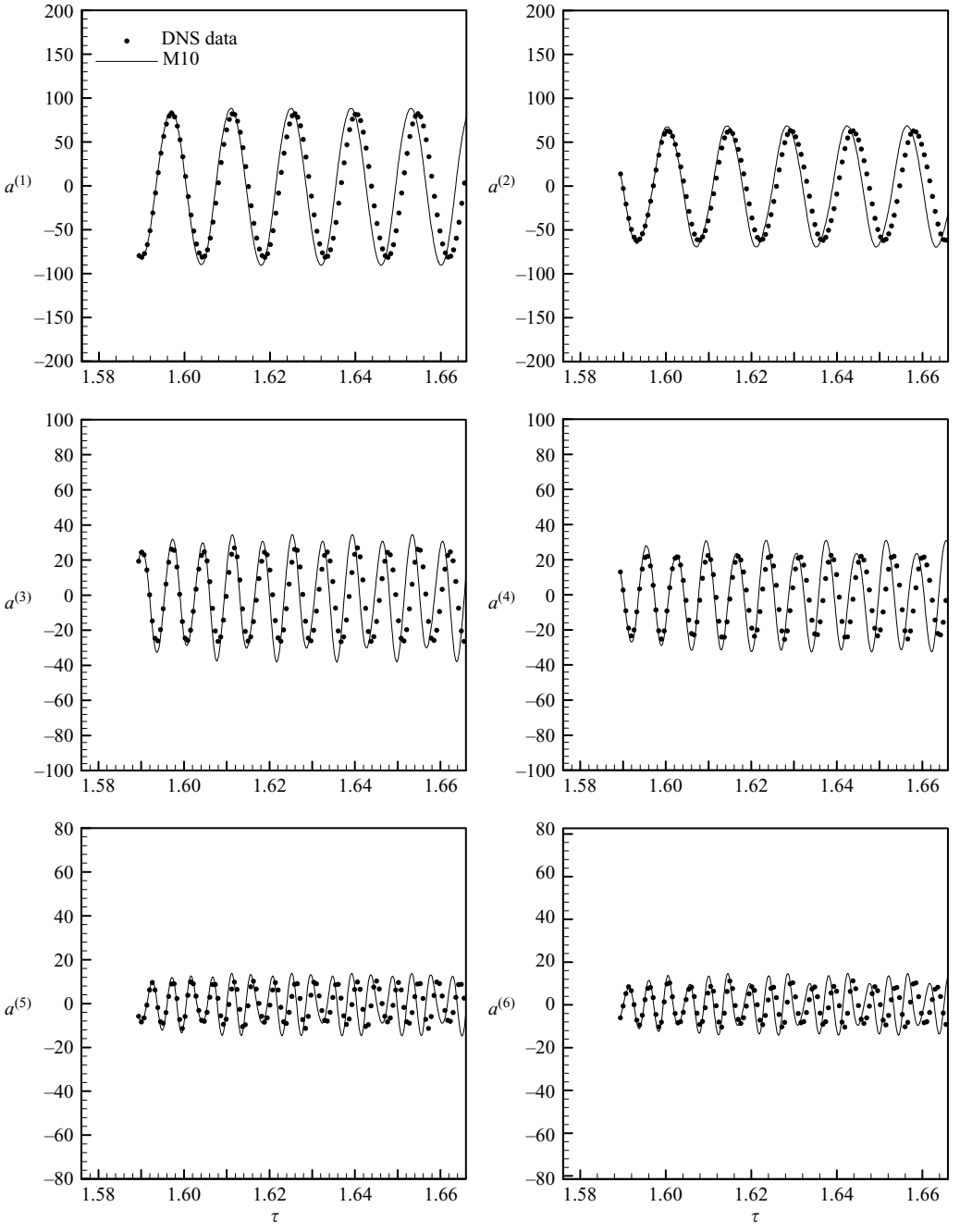

FIGURE 15. Comparison of time histories of the temporal modal coefficients $a^{(1)}$–$a^{(6)}$ obtained from a ten-dimensional model and the computational data for $Ra_\Omega = 10^6$.

the data ensemble, the mean flow field obtained from the data ensemble does not represent the true mean flow field at the target parameter value. The second concern is the value of the correlation term D_p. In the validation studies, it has been shown that the term could be successfully evaluated using the DNS values of the temporal

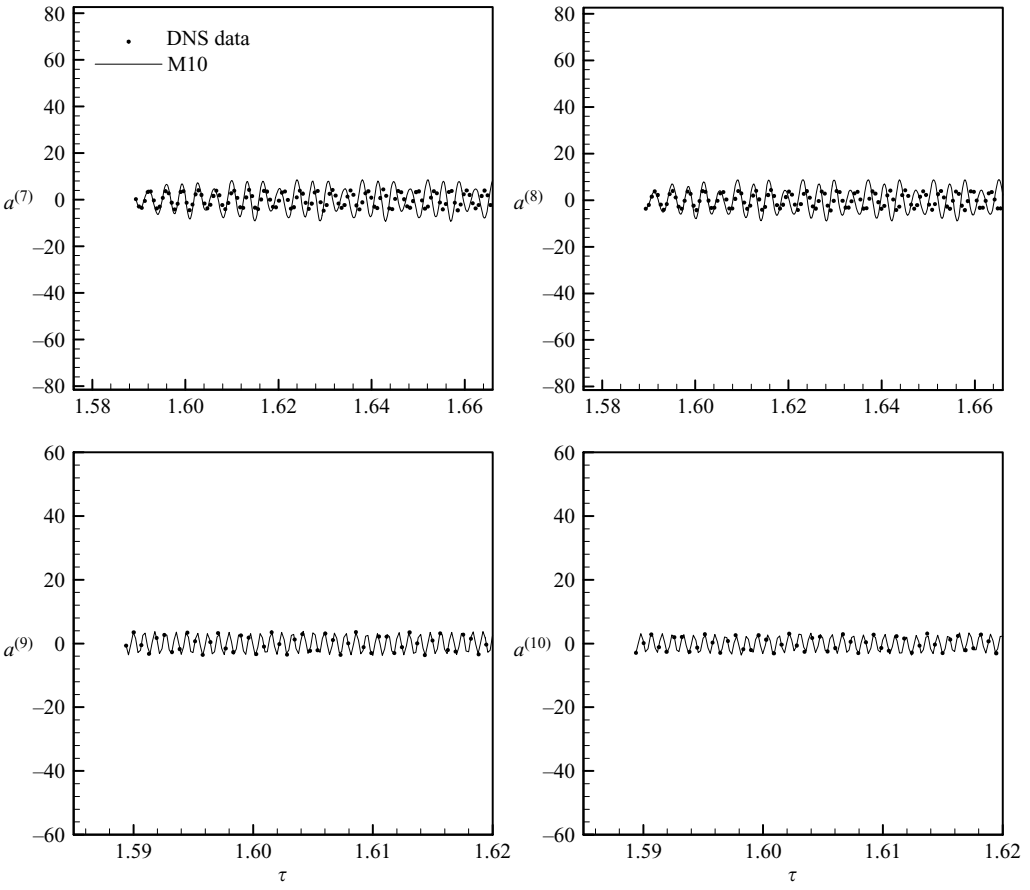

FIGURE 16. Comparison of time histories of the temporal modal coefficients $a^{(7)}$–$a^{(10)}$ obtained from a ten-dimensional model and the computational data for $Ra_\Omega = 10^6$.

coefficients $a^{(p)}$. This in turn would necessitate the use of the DNS data at the target parameter value itself. These issues have a risen because we are dealing with low-dimensional models for the fluctuating flow, for reasons explained in § 3.1.

A simple solution to the mean flow-field issue is to aproximate it as the mean field of the mixed data ensemble. As demonstrated in the validation studies the effect of neglecting the term D_p the low-dimensional model leads to a slight loss of accuracy. Therefore, as a first approximation in the construction of a hybrid model, D_p is simply dropped from the hybrid model. The 50-mode hybrid model constructed in this manner is tested at a target value of $Ra_\Omega = 5 \times 10^2$. Figure 17 compares the time histories of the velocity components and temperature at $(-0.72, 0)$ obtained from integration of the hybrid model without the correlation term D_p, and the full Navier–Stokes simulations. In this simulation the initial condition is supplied in the form of values of $\{a^{(p)},\ p = 1, \ldots, 50\}$ obtained from the numerical data at $Ra_\Omega = 5 \times 10^2$. While there are significant deviations over certain portions of the trajectory, the model predictions agree well qualitatively with the computational predictions in HS. The period of the time histories is found to be 0.0397, which agrees well with the rotation period of 0.0396 dimensionless units of the gravity vector at this Ra_Ω. Thus the frequency-locking is faithfully captured.

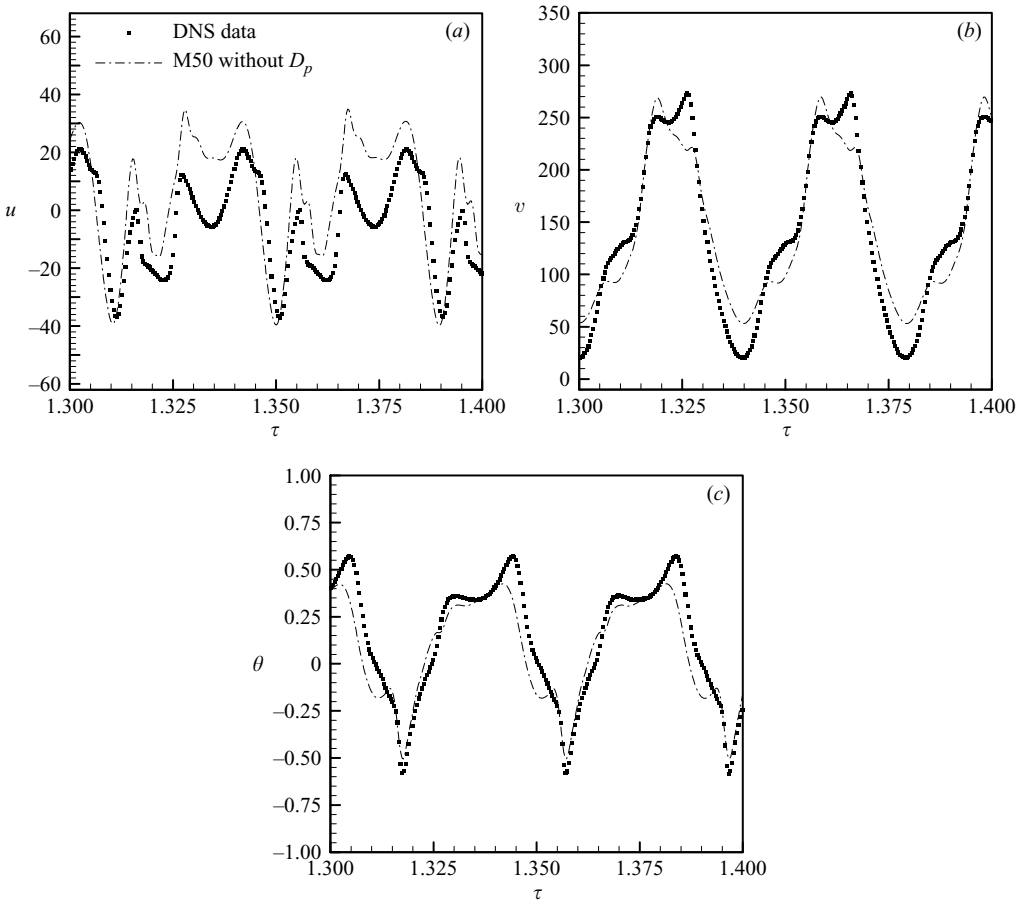

FIGURE 17. Comparison of time histories of (*a*) $u(-0.72, 0)$, (*b*) $v(-0.72, 0)$ and (*c*) $\theta(-0.72, 0)$ obtained from an approximate fifty-dimensional hybrid model (without the term D_p) with the computational data at $Ra_\Omega = 5 \times 10^2$.

Finally, a strategy for incorporating the correlation term D_p in the hybrid model is developed and the performance of the resulting model is assessed. For notational convenience, the two sets of DNS data employed in the hybrid model are denoted as system A ($Ra_\Omega = 10^2$) and system B ($Ra_\Omega = 10^3$). Denote the correlation terms evaluated using the DNS data for these systems as $(D_p)_A$ and $(D_p)_B$ respectively. Then using a simple Lagrange interpolation of first order, one can approximate the value of D_p at any desired parameter in the interval bounded by the parameter values of systems A and B. Symbolically, this may be expressed

$$D_p = \left(D_p\right)_A \left[\frac{P - P_B}{P_A - P_B}\right] + \left(D_p\right)_B \left[\frac{P - P_A}{P_B - P_A}\right]. \tag{21}$$

In (21), P denotes the target value of the parameter while P_A and P_B denote the parameter values corresponding to systems A and B respectively. This strategy is again tested for a 50-mode hybrid model at $Ra_\Omega = 5 \times 10^2$. The results are compared with the full DNS simulations in figure 18. There is a marked improvement in the

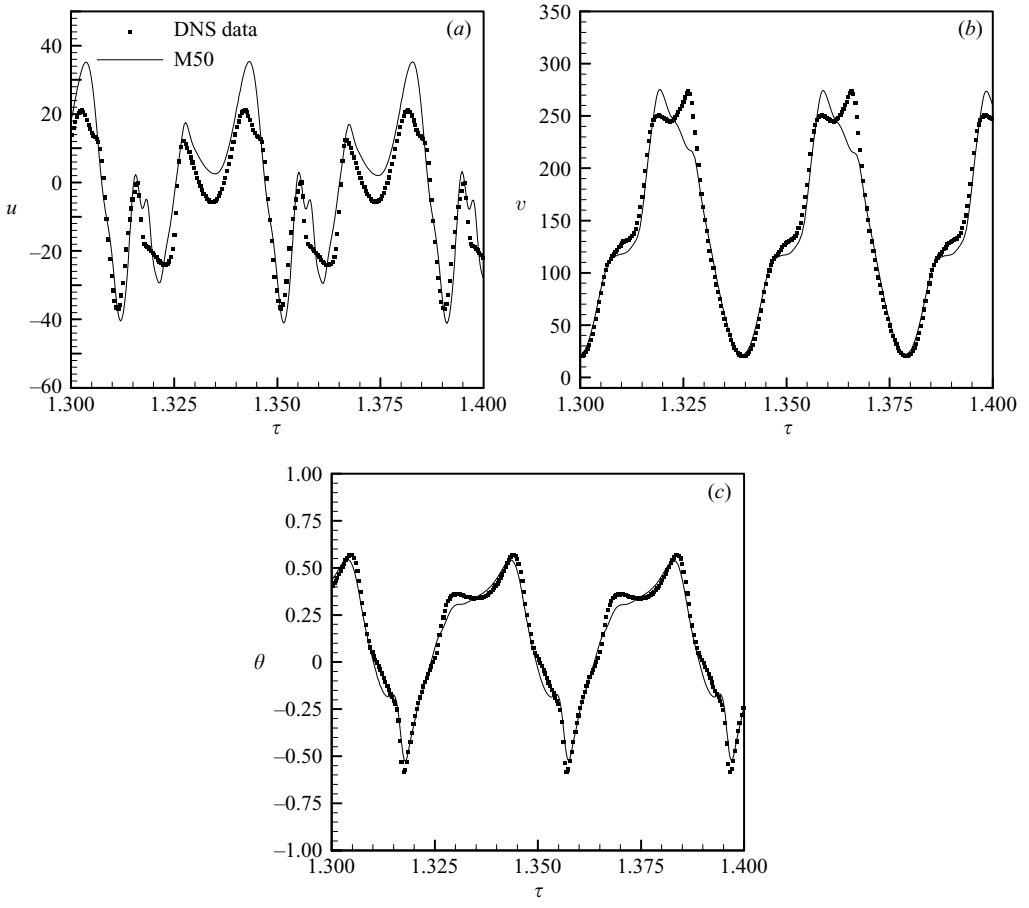

FIGURE 18. Comparison of time histories of (*a*) $u(-0.72, 0)$, (*b*) $v(-0.72, 0)$ and (*c*) $\theta(-0.72, 0)$ obtained from a full fifty-dimensional hybrid model with the computational data at $Ra_\Omega = 5 \times 10^2$.

performance of the hybrid model in comparison to the performance without the correlation term (figure 17). The time histories of velocity and temperature show good agreement over most of the trajectories. The initial data for time integration of this model have been supplied by utilizing the computational data at $Ra_\Omega = 10^2$ instead of taking a snap of the flow field at $Ra_\Omega = 5 \times 10^2$. After an initial transient period which corresponds to approximately five 'g' cycles, the hybrid model captures the long-term behaviour of the flow faithfully.

The hybrid model constructed in the manner described above is expected to perform well across a range of parameters for which the mean flow field and the structure of the fluctuations are relatively insensitive or vary slowly with changes in the parameter (Ra_Ω). For ranges where large changes in the mean and the fluctuating field are expected, the strategy proposed in the current work could be extended with data sampled at a larger number of parameter values spanning the range of interest. This would capture the trend of the mean flow field as well as the fluctuations more accurately. The term D_p could also be obtained using higher-order Lagrange interpolations capturing the nonlinear trends in a more accurate manner.

4. Conclusions

The present study demonstrates the effectiveness of POD as a tool for the analysis of a complex fluid flow involving unsteady flow with heat transfer. It has been demonstrated that relatively few modes are needed to capture the structure of the unsteady flow field within a specified level of accuracy. A different criterion for specifying the accuracy of reconstructions based on POD modes, that directly reflects the accuracy to which the spatio-temporal structure of a given data ensemble can be represented, has been proposed.

The presence of travelling waves in the flow has been detected by employing POD on the computational data at $Ra_\Omega = 10^3$ and $Ra_\Omega = 10^6$. At $Ra_\Omega = 10^3$, the waves propagate predominantly in the circumferential direction in the clockwise manner and are believed to be caused by the interaction between the gravitational buoyancy, the fluid inertia and the viscous forces. These travelling waves are found to exist for values of Ra_Ω in the range $10^3 - 1.9 \times 10^3$. The space–time symmetry of the degenerate pairs of modes is utilized to estimate the average circumferential wave speeds for these cases. For $Ra_\Omega = 10^6$, the flow is dominated by the centrifugal buoyancy and the gravitational buoyancy has a very weak influence on the flow field. Travelling waves are also found in the flow field at this Ra_Ω. These waves appear to propagate together with the strong convective current from the hot end towards the cold end of the horizontal diameter with respect to the rotating observer.

Low-dimensional models based on POD modes have been constructed and issues involved in their closure arising out of the specific nature of the problem under consideration have been successfully resolved. An important aspect of POD analysis that has not been given due importance for non-isothermal flows is the definition of the inner product space in which the combined decomposition of velocity and temperature field is desired. It has been shown that for situations where the order of magnitude of the velocity and the temperature fields is not comparable, the choice of the proper value of the scaling factor γ is critical to the success of the low-dimensional model. Having included a sufficient number of modes in the low-dimensional models so that a sufficient amount of dissipation is present to stabilize their solution for several hundred rotation cycles of the gravity vector, not more than 20 mode models were required to accurately capture the temporal dynamics of the system for the five cases under consideration.

A procedure for constructing a hybrid low-dimensional model aimed at capturing the flow dynamics over a range of parameter values has been suggested. The procedure has been tested by constructing the model from a mixed database of an equal number of snapshots at $Ra_\Omega = 10^2$ and $Ra_\Omega = 10^3$ and using it to reproduce the flow dynamics at $Ra_\Omega = 5 \times 10^2$. The results obtained accurately predict the period of flow using the low-dimensional model. While the proposed strategy appears to be simple, it has the potential of refinement, and its effectiveness and robustness need to be investigated.

Appendix

The various coefficients in (20) are defined as

$$L_{pr}(\tau) = L_{pr}^{GB}(\tau) + L_{pr}^{CF} - L_{pr}^{RB} + L_{pr}^{V} - L_{pr}^{M},$$

$$L_{pr}^{GB}(\tau) = Ra_g Pr \left(L_{pr}^{GB1} \sin\left(Ta^{1/2} Pr\tau\right) + L_{pr}^{GB2} \cos\left(Ta^{1/2} Pr\tau\right) \right),$$

$$L_{pr}^{GB1} = \int \phi_1^{(p)} \phi_3^{(r)} \, \mathrm{d}A, \quad L_{pr}^{GB2} = \int \phi_2^{(p)} \phi_3^{(r)} \, \mathrm{d}A,$$

$$L_{pr}^{RB} = Ra_{\Omega} Pr \int \left(x\phi_1^{(p)} + y\phi_2^{(p)}\right)\phi_3^{(r)}\,\mathrm{d}A,$$

$$L_{pr}^{CF} = 2Ta^{1/2} Pr \int \left(\phi_1^{(p)}\phi_2^{(r)} - \phi_2^{(p)}\phi_1^{(r)}\right)\mathrm{d}A,$$

$$L_{pr}^{M} = \int \left\{ \phi_i^{(p)} \left(\phi_j^{(r)} \frac{\partial U_i}{\partial x_j} + U_j \frac{\partial \phi_i^{(r)}}{\partial x_j} \right) + \gamma \phi_3^{(p)} \left(\phi_j^{(r)} \frac{\partial U_3}{\partial x_j} + U_j \frac{\partial \phi_3^{(r)}}{\partial x_j} \right) \right\} \mathrm{d}A,$$

$$L_{pr}^{V} = \int \left\{ Pr\phi_i^{(p)} \frac{\partial^2 \phi_i^{(r)}}{\partial x_j \partial x_j} + \gamma \phi_3^{(p)} \frac{\partial^2 \phi_3^{(r)}}{\partial x_j \partial x_j} \right\} \mathrm{d}A,$$

$$Q_{prs} = \int \left\{ \phi_i^{(p)} \phi_j^{(r)} \frac{\partial \phi_i^{(s)}}{\partial x_j} + \gamma \phi_3^{(p)} \phi_j^{(r)} \frac{\partial \phi_3^{(s)}}{\partial x_j} \right\} \mathrm{d}A,$$

$$F_p(\tau) = A_p \sin\left(Ta^{1/2} Prt\right) + B_p \cos\left(Ta^{1/2} Prt\right) + C_p - D_p,$$

$$A_p = Ra_g Pr \int \phi_1^{(p)} U_3\,\mathrm{d}A, \quad B_p = Ra_g Pr \int \phi_2^{(p)} U_3\,\mathrm{d}A,$$

$$C_p = \lambda^{(r)} \int \left\{ \phi_i^{(p)} \phi_j^{(r)} \frac{\partial \phi_i^{(r)}}{\partial x_j} + \gamma \phi_3^{(p)} \phi_j^{(r)} \frac{\partial \phi_3^{(r)}}{\partial x_j} \right\} \mathrm{d}A,$$

$$D_p = Ra_g Pr \left\{ \left\langle L_{pr}^{GB1} a_{DNS}^{(r)} \sin\left(Ta^{1/2} Prt\right) \right\rangle + \left\langle L_{pr}^{GB2} a_{DNS}^{(r)} \cos\left(Ta^{1/2} Prt\right) \right\rangle \right\}.$$

In the above definitions, the integrals are to be evaluated over the entire domain D of the flow field. The subscripts $(i, j) \in [1, 2]$ and summation over repeating indices is implied.

REFERENCES

Aubry, N. 1991 On the hidden beauty of the proper orthogonal decomposition. *Theor. Comput. Fluid Dyn.* **2**, 339–352.

Aubry, N., Guyonnet, R. & Lima, R. 1992 Spatio-temporal symmetries and bifurcations via Bi-Orthogonal decompositions. *J. Nonlin. Sci.* **2**, 183–215.

Aubry, N., Holmes, P., Lumley, J. L. & Stone, E. 1988 The dynamics of coherent structures in the wall region of a turbulent boundary layer. *J. Fluid Mech.* **192**, 115–173.

Aubry, N. & Lian, W. Y. 1993 *Exploiting and Detecting Space-time Symmetries.* Lectures in Applied Mathematics, vol. 29, pp. 71–85. Springer.

Aubry, N. & Lima, R. 1995 Spatiotemporal and statistical symmetries. *J. Stat. Phys.* **81**(3/4), 793–828.

Bakewell, P. & Lumley, J. L. 1967 Viscous sublayer and adjacent wall region in turbulent pipe flows. *Phys. Fluids* **10**, 1880–1889.

Cazemier, W., Verstappen, R. W. C. P. & Veldman, A. E. P. 1998 Proper Orthogonal decomposition and low-dimensional models for driven cavity flows. *Phys Fluids* A **10**(7), 1685–1699.

Deane, A. E. & Sirovich, L. 1991 A computational study of Rayleigh-Bénard convection. Part 1. Rayleigh number scaling. *J. Fluid Mech.* **222**, 231–250.

Galletti, B., Bruneau, C. H., Zannetti, L. & Iollo, A. 2004 Low order modelling of laminar flow regimes past a confined square cylinder. *J. Fluid Mech.* **503**, 161–170.

Glauser, M. N. & George, W. K. 1987 Orthogonal decomposition of the axisymmetric jet mixing layer including azimuthal dependence. *Advances in Turbulence*, pp. 357–366, Springer.

Hamady, F. J., Lloyd, J. R., Yang, K. T. & Yang, H. Q. 1994 A study of natural convection in a rotating enclosure. *Trans. ASME: J. Heat Transfer* **116**(1), 136–143.

Hasan, N., Anwer, S. F. & Sanghi, S. 2005 On the outflow boundary condition for external incompressible flows: a new approach. *J. Comp. Phys.* **206**, 661–683.

Hasan, N. & Sanghi, S. 2004 The dynamics of two-dimensional buoyancy driven convection in a horizontal rotating cylinder. *Trans. ASME: J. Heat Transfer* **126**(6), 963–984.

Herzog, S. 1986 Large scale structure in the near wall region of a turbulent pipe flow. PhD thesis, Cornell University.

Hirsch, C. 1990 *Numerical Computation of Internal and External Flows*, pp. 661–664. John Wiley and Sons Ltd.

Holmes, P., Lumley, J. L. & Berkooz, G. 1996 *Turbulence, Coherent Structures, Dynamical Systems and Symmetry*, pp. 88–91. Cambridge University Press.

Ker, Y. T. & Lin, T. F. 1996 A combined numerical and experimental study of air convection in a differentially heated rotating cubic cavity. *Intl J. Heat Mass Transfer* **39**(15), 3193–3210.

Kirby, K., Boris, J. & Sirovich, L. 1990 An eigenfunction analysis of axisymmetric jet flow. *J. Comp. Phys.* **90**(1), 98–122.

Lumley, J. L. & Poje, A. 1997 Low-dimensional models for flows with density fluctuations. *Phys. Fluids* **9**, 2023–2031.

Ma, X. & Karniadakis, G. E. 2002 A low-dimensional model for simulating three-dimensional cylinder flow. *J. Fluid Mech.* **458**, 181–190.

Moin, P. & Moser, R. D. 1989 Characteristic-eddy decomposition of turbulence in a channel. *J. Fluid Mech.* **200**, 471–509.

Podvin, B. & Quéré, P. L. 2001 Low-order models for the flow in a differentially heated cavity. *Phys. Fluids* **13**, 3204–3214.

Rempfer, D. 2000 On low-dimensional Galerkin models for fluid flow. *Theor. Comp. Fluid Dyn.* **14**(2), 75–88.

Rempfer, D. & Fasel, H. 1994 Evolution of three-dimensional coherent structures in a flat plate boundary layer. *J. Fluid Mech.* **260**, 351–375.

Sahan, R. A., Liakopoulos, A. & Gunes, H. 1997 Reduced dynamical models of nonisothermal transitional grooved-channel flow. *Phys. Fluids* **9**, 551–565.

Sanghi, S. & Aubry, N. 1993 Mode interaction models for near-wall turbulence. *J. Fluid Mech.* **247**, 455–488.

Sirovich, L. 1987 Turbulence and the dynamics of coherent structures. Part I. Coherent structures. *Q. Appl. Maths* **45**(3), 561–571.

Sirovich, L. & Deane, A. E. 1991 A computational study of Rayleigh-Bénard convection. Part 2. Dimension considerations. *J. Fluid Mech.* **222**, 251–265.

Sirovich, L. & Park, H. 1990 Turbulent thermal convection in a finite domain, Part I. Theory. *Phys. Fluids* A **2**, 1649–1658.